ABSTRACT

Title of Thesis:	ELECTROCHEMICAL PHASE ENGINEERING AND THREE-DIMENSIONAL NANOPORE ARCHITECTURES FOR ADVANCED SODIUM-ION MICROBATTERY SYSTEMS
	Zihan Sun, Doctor of Philosophy, 2026
Thesis Directed By:	Professor Sang Bok Lee, Department of Chemistry & Biochemistry

The rapid depletion of fossil fuels and the increasing demand for large-scale energy storage systems have accelerated the development of sodium-ion batteries (SIBs) as a cost-effective alternative to lithium-ion systems. The sluggish kinetics of large sodium-ion intercalation and short cycle lifetime have bothered researchers so far. This thesis presents a novel strategy to overcome these challenges through the integration of semiconductor-compatible synthesis method and 3D nanostructuring.

First, a scalable and "green" synthesis route is demonstrated for the metastable γ'-V_2O_5 crystal. Unlike traditional methods involving hazardous reagents or extreme conditions, this approach utilizes a two-step process: the conformal growth of V_2O_5 thin films via ALD followed by precise electrochemical lithium-ion insertion to induce a phase transformation. The resulting γ'-V_2O_5 electrodes exhibit superior sodium-storage properties, including a high specific capacity of 147 mAh/g and distinct high-voltage plateaus that are absent in the α phase.

To further address the kinetic limitations inherent in sodium-ion storage, we transfer from planar thin-film geometries to 3D nanopore architectures. By utilizing anodic aluminum oxide (AAO) templates, 3D coaxial nanotubular electrodes were fabricated, significantly increasing the active surface area and shortening ion diffusion paths. This architectural optimization resulted in a tenfold improvement in cycling stability, maintaining 80% capacity retention over 720 cycles.

Additionally, the compatibility of the 3D nanoporous architecture that we developed in 2nd work with solid-state electrolytes was explored, demonstrating a pathway toward high-performance, safe, and integrable solid-state sodium-ion microbatteries. Collectively, this research provides a comprehensive framework for tuning electrode phases and architectures at the nanoscale, offering a viable blueprint for the next generation of high-power sodium-ion energy storage devices.

ELECTROCHEMICAL PHASE ENGINEERING AND THREE-DIMENSIONAL NANOPORE ARCHITECTURES FOR ADVANCED SODIUM-ION MICROBATTERY SYSTEMS

by

Zihan Sun

Thesis submitted to the Faculty of the Graduate School of the
University of Maryland, College Park, in partial fulfillment
of the requirements for the degree of
Doctor of Philosophy
2026

Advisory Committee:
Professor Sangbok Lee, Chair
Professor Gary Rubloff
Professor Xiaodong Mike Shi
Professor Yuhuang Wang
Professor Zhiwei Li
Dr. Keith Gregorczyk

Acknowledgements

I would like to begin by expressing my deepest gratitude to my advisor, Professor Sang Bok Lee, for his invaluable guidance, patience, and support throughout this research journey. His profound knowledge of electrochemistry and semiconductor processing thecniques, combined with his vision for the future of 3D microbatteries, has been the cornerstone of this work. I am truly honored to have been a part of our research group and to have learned from his commitment to excellence.

I am also sincerely grateful to Dr. Keith E. Gregorczyk and Dr. Nam S. Kim for their mentorship and technical expertise, particularly regarding the development of Atomic Layer Deposition (ALD) processing and fabrication of 3D microbatteries that were essential to this program.

Special thanks go to my lab mates and Professor Gary Rubloff's research group members for creating a stimulating and collaborative research environment. I would like to thank Professor Gary Rubloff's support throughout my program. His expertise in material science helped a lot with my study on nanomaterials. I specifically want to thank Steven M. Douglass, Osma J. Gomez, Daniela R. Fontecha and George C. Caceres for their help with experimental setups and many hours of fruitful discussion. The collective expertise of our group on nanostructured systems and sodium ionics provided the perfect platform for this dissertation.

I am indebted to the staff of the nanofabrication and characterization facilities for their technical support with the Beneq TFS500 ALD platform, the AJA ATC 1800 Sputtering unit, and the Rigaku SmartLab diffractometer. Their assistance was vital in ensuring the structural integrity and precision of the nanostructured electrodes presented in this work. I would like to thank Dr.

David Zitoun, R. Tiwari, and R. B. Nuwayhid for their insightful collaboration and contributions to the fundamental understanding of γ'-V_2O_5 synthesis mechanisms.

This research was supported by the U.S. Department of Energy (DOE) Advanced Materials and Manufacturing Technologies Office (AMMTO) under a grant focused on the integration of 3D microbatteries into anodic aluminum oxide (AAO) templates. I am grateful for their financial support, which made this ambitious scaling project possible.

Finally, I would like to thank my family and friends. To my parents, thank you for your unconditional love and for always encouraging me to pursue my academic goals, thank you for your unwavering support and for standing by me through the challenges of the PhD process. This achievement is as much yours as it is mine.

Table of Contents

Chapter 1: Introduction

1.1 Motivation

The development of modern society continues consuming unrenewable fossil fuels including petroleum, natural gas, coal, etc. Amid the rapid depletion of fossil fuel resources and mounting global pollution, renewable energy is emerging as a viable alternative to fossil fuels.[1,2]. Renewable energy sources contain solar energy, wind energy, etc. These energy sources are usually intermittent and easy to be affected by weather, increasing the difficulty for the practical application. Therefore, reliable energy storage and conversion techniques are required to make full use of sustainable energy sources. Within couple existing energy storage systems, the fast advancement of battery technology, especially lithium-ion batteries (LIBs), featuring high energy density and flexible volumetric capacity, makes batteries play an important role in energy utility evolution process.

The earliest commercialization of LIBs can be tracked back to 1991 and chosen to be the energy source for portable electronics[3]. Recent development of electric vehicles and massive energy storage devices spurs the rapidly increasing requirements of lithium resources, which have, however, scarcity and uneven distribution on earth. The costly price of lithium resources seriously affects the market of LIBs. In order to offset the impact from frequent fluctuation of lithium price, sodium-ion batteries (SIBs) went back into researchers' sight again. As a matter of fact, commercial SIBs have already been developed in 1980s, but the relative research has been trapped for almost 20 years due to its lower energy density than LIBs. SIBs have rapidly evolved recently because of the following advantages over LIBs: (1) sodium resources on earth are much more

abundant than lithium resources, leading to lower price; (2) higher safety than LIBs; and (3) lower capacity degradation under low temperature[4,5].

Although sodium-ion batteries promise a cheaper, more earth-abundant route to large-scale energy storage, they are held back by a series of problems: sluggish sodiation kinetics and large lattice strain, poor electronic conductivity in many high-voltage cathodes[6,7], and catastrophic volume change in high-capacity anodes[8]. These issues translate into low initial efficiency, rapid capacity fade, and trade-off between capacity and power performance when conventional, bulk materials are used. To solve these problems, nanostructuring design offers a solution. 3D porous and core–shell architectures were created to enlarge active surface area, shorten ion-diffusion pathways, and accommodate mechanical strain, delivering faster kinetics, higher usable capacity, and far better cycle life[9–11]. Additionally, conductive carbon or metal networks coupled with transition-metal oxides or polyanions can be intimately integrated into these nanostructures. For SIBs to move from laboratory promise to grid-scale reality, the field must therefore pivot from traditional bulk chemistries to engineered nanoscale architectures that reconcile capacity, stability and safety.

Among the synthesis methods to prepare nanostructured electrode materials, Atomic-layer deposition (ALD) is a promising technique, providing angstrom-to-nanometer control over surface of substrates that simultaneously keep material morphology and guarantee interfacial contact within stacked layers[12]. Additionally, the self-limiting nature of ALD and the saturated surface reactions also allow ALD to deposit coating with high conformity and precise thickness controllability on high aspect ratio surfaces[13]. The cycle-by-cycle growth mode enables precise mass and thickness control, minimizing inactive coating weight while engineering ion-conductive

or mechanically resilient interlayers, so that electrodes gain improved rate capability, suppressed transition-metal dissolution and far superior cycling stability.

In sodium ion systems, by depositing ultrathin oxides, oxynitrides and mixed-phase films onto anodes, cathodes and solid-state electrolytes, ALD forms stable artificial SEI/CEI layers that suppress parasitic reactions and tailors nanoscale architectures (core–shells, inverse opals, conformal shells on nanowires or nanopillars) that shorten Na^+ diffusion paths and accommodate volume change[14–16]. Overall, ALD converts problematic bulk materials into functional nanostructures by controlling chemistry, thickness and morphology at the atomic scale, thereby addressing the kinetic and stability limitations that have hindered SIB performance. Throughout my program, I've developed an electrochemical phase engineering method to synthesize γ'-V_2O_5 and fabricated 3D nanopore sodium-ion microbatteries with γ'-V_2O_5 electrodes. ALD technique plays an important role in both works. The tuned and controllable features of ALD help us build the electrochemical test platform to push the boundary of our understanding on sodiation within nano-scale environment. It'll also help us in future research on solid-state microbatteries.

1.2 Thesis Overview

According to our group's long-time research[17–22] on nanostructured Li-ion batteries, the nanoscale architecture design brings excellent electrochemical performance to LIBs. We believe that it'll also have similar effects on Na-ion system which would help us fabricate ideal SIBs. To deepen our understanding of nano-scale SIBs, the architectural elements including crystalline phase of materials and nanostructures were explored. In the beginning of this program, we've developed an electrochemical phase engineering method to synthesize γ'-V_2O_5 which has appropriate crystalline phase for sodiation. The microbatteries with nanopore structures were then fabricated, featuring high capacity, long cycle lifetime, and high-power performance. In the end,

we also explored the possibility to integrate solid-state electrolytes into 3D nanopore microbatteries to eventually make solid-state microbatteries. The whole program is divided into three phases, and we are going to answer the following questions:

1) Can a high-voltage, high-capacity cathode be synthesized for SIBs using semiconductor-compatible methods? (Chapter 3).

2) Can nanostructuring overcome the kinetic limitations of large-ion (Sodium) storage? (Chapter 4).

3) Can these materials and architectures support the transition to solid-state sodium-ion microbatteries? (on-going, Chapter 5).

1.3 Review of Cathode Materials for Sodium Ion Batteries

As outlined earlier in the thesis, we believe the semiconductor-compatible synthesis method and nano-structuring can support the fast kinetics in sodium-ion systems, and further transition into 3D nanostructured solid-state sodium-ion batteries which feature high capacity, long cycle lifetime, high power performance, and safety. Achieving this goal requires not only a deep understanding of the electrode materials that fundamentally govern ion storage, redox behavior, and long-term stability, but also architectural innovation such as high-aspect-ratio nanopores, conformal ALD coatings, and integrated current collectors. In solid-state microbattery design, where ionic pathways are short and interfacial contact is critical[17,19], the choice of cathode material becomes even more consequential.

Solid-state microbatteries impose stringent demands on cathode chemistry. Unlike bulk or slurry-cast electrodes, microbattery cathodes must operate reliably in nanoconfined geometries, maintain structural integrity under repeated cycling, and form stable interfaces with solid

electrolytes such as NaPON[23] or polymerized DOL[24]. These constraints amplify the intrinsic challenges already present in sodium-ion systems, including slower Na^+ diffusion kinetics, larger ionic radius, and distinct interfacial chemistry compared to lithium-ion analogues. As noted in literature, current sodium-ion batteries face sluggish sodiation kinetics, large lattice strain, poor electronic conductivity in many high-voltage cathodes, and catastrophic volume change in high-capacity anodes[25,26], all of which directly influence cathode selection and design. For solid-state architectures, where interfacial impedance and mechanical compatibility are dominant failure modes[23], cathode materials must offer both high redox activity and structural resilience.

Within this context, reviewing cathode materials for sodium-ion batteries is essential for identifying sodium chemistries that can be successfully integrated into 3D solid-state microbattery platforms. The field has explored a wide range of candidates—from Prussian blue analogues to layered transition-metal oxides and polyanionic frameworks—each with distinct advantages and limitations. However, many conventional SIB cathodes were developed for bulk, liquid-electrolyte cells and do not readily translate to nanoscale, solid-state environments. For example, layered oxides often undergo complex phase transitions during Na^+ insertion[27], while polyanionic materials may suffer from low electronic conductivity or limited voltage windows[28]. These issues highlight the need for cathode materials that combine high theoretical capacity, stable Na^+ intercalation pathways, and compatibility with thin-film or nanostructured fabrication methods.

Since the large-scale adoption of lithium-ion batteries (LIBs) in portable electronics and electric vehicles, the price and availability of lithium have fluctuated wildly[29]. The abundance of sodium has therefore made sodium-ion batteries (SIBs) attractive as a potential complement or replacement for all LIBs fields including microbattery area for small electronic devices[30,31]. Fundamentally the physics and chemistry of LIBs are the same as SIBs, leading to many attempts

at deriving SIB electrodes from LIB systems[32]. However, the design of electrode materials for SIBs with high performance remains a challenge.

$LiCoO_2$, and its cobalt-substituted derivatives (i.e. NMC, NCA, etc.), have been shown to be a mature cathode material in LIBs but shows multiphase transformations in SIBs during charge-discharge process, leading to poor cycle stability[27,33]. In addition the extraction costs of cobalt, both financial and social, is another factor that cannot be ignored during commercialization[34].

The most successful SIB cathode to date has been Prussian blue (PB, $KFe[Fe(CN)_6]\cdot nH_2O$) and its analogs (PBAs). These transition metal cyanides have crystal structures with vacancies in the framework that store and conduct sodium ions[35,36]. Multiple companies have commercialized versions of this SIB chemistry, demonstrating a working voltage of 1.56 V, initial capacity of 67 mAh/g, and a cycle stability greater than 4000 cycles[37]. Although SIBs based on PBAs have been commercialized, the low working voltage and small specific capacity limit their application space.

Beyond PBAs, vanadium oxides (i.e., VO_2, V_2O_3, V_2O_5, V_3O_8, etc) are considered to be next-generation cathode materials for SIBs because of their fast ion-diffusion enabled by a layered crystal structure and excellent electrochemical properties resulting from diverse oxidation redox couples from V^{2+} to V^{5+} [28,38,39]. Among vanadium oxides, V_2O_5 is of great interest since the large interlayer space allows intercalation and deintercalation of various cations including Li^+, Na^+ and Mg^{2+} [40–42]. Additionally, V_2O_5 exhibits many stable crystal structures, differing in cation acceptability, cycle stability with the chosen cation, and ultimately the power and energy delivered[43]. Within the crystal system of V_2O_5, α-V_2O_5 is popular LIB cathode due to the high theoretical capacity of 440 mAh/g when each unit formula contains three lithium ions (i.e., $Li_3V_2O_5$) and displays a phase-transition process as a function of lithium ions concentration (i.e. state of charge)[22,44,45].

Similar to the LCO case, it was expected that excellent performance in LIBs would translate into success in SIBs[46]. However, the mechanism of sodium insertion into α-V_2O_5 was investigated and shown to be quite different from lithium insertion[47]. The initial sodiation plateau showed a phase transformation at ~1.8 V (vs. Na/Na^+) or ~2.1 V (vs. Li/Li^+) during discharging, which is much lower than lithium insertion (3.2 V vs. Li/Li^+)[22]. Furthermore, charge-discharge cycling showed low Coulombic efficiency further confirming the difficulty of sodium insertion into α-V_2O_5 [47]. Though it was shown cycling could be improved by cycling between NaV_2O_5 and $Na_2V_2O_5$ (0.8~1.5 V vs. Na/Na^+), poor rate performance continues to limit application[48].

Vanadium-based oxides, particularly V_2O_5 and its polymorphs, have emerged as promising candidates because of their layered structures, multivalent redox chemistry, and ability to accommodate larger sodium ions[46]. As literature demonstrates, γ′-V_2O_5, a specific polymorph of V_2O_5, offers a unique combination of high working voltage and reversible Na^+ intercalation ability which attract our attention. γ'-V_2O_5 also has an orthorhombic layered structure. Since γ'-V_2O_5 has a larger interlayered spacing (4.9 Å) than α-V_2O_5 (4.37 Å), sodium ions have shown relatively easy insertion into γ'-V_2O_5 to generate γ-NaV_2O_5, with the phase transition plateau at 3.4V (vs Na/Na^+) or 3.6 V (vs. Li/Li^+)[49]. The sodium-insertion process from γ'-V_2O_5 to γ-NaV_2O_5 proceeds via a two-step process: (1) two phases which include γ'-V_2O_5 and γ-$Na_{0.7}V_2O_5$ ($0 < x \leq 0.7$) coexist in the material; (2) only a single phase of γ-$Na_xV_2O_5$ ($0.7 < x \leq 0.97$) exists in the crystal. The cycling of charge-discharge shows a discharge specific capacity of 152 mAh/g which is consistent with, though slightly higher than, the theoretical value (147 mAh/g), and this capacity is reversible for multiple cycles[49–52].

Another polymorph of V_2O_5, β-V_2O_5, also has the ability to store sodium ions. The sodium insertion into β-V_2O_5 is divided into three steps: (1) a solid solution region in 3.1-3.2 V (vs. Na/Na^+)

and β-$Na_xV_2O_5$ ($0.35 < x \leq 0.45$) region; (2) β-$Na_xV_2O_5$ ($0.65 < x \leq 0.7$) region; (3) β-$Na_xV_2O_5$ ($0.9 < x \leq 1$) region. Step (1) corresponds to a peak at 3.1 V (vs. Na/Na^+) in cyclic voltammograms while the step (2) and (3) correspond to peaks at 2.6 V (vs. Na/Na^+). Although both γ'-V_2O_5 and β-V_2O_5 show excellent performance of sodium storage, the preparation methods are demanding.

In the early stages of this program, we hope the electrode materials can be prepared by ALD-based thin-film synthesis method using the experience from our group's research on ALD technique[18,19,22,53]. If possible, the morphology of the electrode materials can be tuned to fit the integration into a nanoscale system. Thus, before advancing toward fully solid-state microbattery integration, we've surveyed the broader landscape of sodium-ion cathode materials, understand their electrochemical behavior, and then positioned γ'-V_2O_5 within this framework. The conventional preparation methods of γ'-V_2O_5 usually require high temperature and toxic chemicals. For instance, carbothermal reduction synthesis of γ-LiV_2O_5 requires temperatures of 600 ℃ and chemical oxidation with highly toxic NO_2BF_4[51]. Another cathode material, β-V_2O_5, needs not only high temperature of 800 ℃ but additionally high pressure of 4 GPa for preparation[54]. Since the current preparation methods for γ'-V_2O_5 and β-V_2O_5 are highly demanding, developing a facile synthesis route to prepare thin film V_2O_5 material for sodium storage is needed.

In chapter 3, we present a method we refer to as electrochemical phase engineering to prepare γ'-V_2O_5 by combining thin-film material synthesis (i.e. atomic layer deposition, ALD), thermal annealing, and wet-chemical electrochemistry. Compared with conventional synthesis methods discussed above, the method presented here can be finished under mild conditions, at low temperature (250 ℃), without the use of highly toxic chemicals, and requires no external pressure. Additionally, we compare the electrochemical performance of γ'-V_2O_5 and α-V_2O_5 thin films as

cathodes in SIBs. Our synthesized γ'-V_2O_5 thin film achieved the theoretical specific capacity (147 mAh/g) when discharged at 0.1 C-rate without the need of any binders or conductive additives and has an exceptional coulombic efficiency of 98%, significantly surpassing previously reported values (~50% CE). The sodium insertion and deinsertion reactions in γ'-V_2O_5 were stable when charge-discharge rate increased to 2 C, exhibiting a similar rate performance with γ'-V_2O_5 powder. Therefore, this work provides a facile and safe method to prepare γ'-V_2O_5 thin films which is confirmed to be a promising cathode material for SIBs. Since the morphology of thin film γ'-V_2O_5 is determined by the substrate, this method enables us to control its morphology by using different substrates, which makes it possible to establish various electrochemistry platforms based on different morphologies of γ'-V_2O_5 for future electrochemical research.

1.4 Review of Nanostructured Sodium Ion Batteries

The three-dimensional nanoscale architectures developed in semiconductor manufacturing to overcome area and volume-limited device metrics such as capacitance, gate density, and interconnect resistance have recently emerged as a powerful solution for similarly constrained electrochemical systems[55]. Our group and others have shown that high-aspect-ratio architectures dramatically enhance ion transport, enabling faster lithiation kinetics, higher areal and volumetric energy and power densities, and scaling relationships that parallel those long established in microelectronics[17,56]. By confining charge storage and transport within defined nanoscale geometries and maintaining intimate contact among device components, power and energy densities can be tuned independently, and ionic functionality can be incorporated into traditionally

electronic or capacitive device platforms. Together, these results demonstrate not only that precision semiconductor manufacturing can be brought directly into the electrochemical device space, but also that ionic materials and architectures can enable new functionalities for board-level signal and energy manipulation. This architectural perspective has already influenced conventional battery manufacturing, where thin-film coatings originating from semiconductor processes are now routinely applied to powder-based electrodes in advanced transportation and consumer battery systems and are considered value additive, marking an important early step toward broader integration of semiconductor fabrication into battery production[57].

Despite the success of semiconductor-derived architectural strategies in lithium-ion systems[58,59], their extension to sodium-ion systems has been limited. Sodium is an attractive alternative to lithium, approximately one thousand times more abundant and offering comparable redox chemistry as other monovalent alkali metals[60,61,62], leading to the expectation that many LIB materials and fabrication approaches would translate seamlessly. Yet in practice, the opposite has been true. Although the governing electrochemical equations for Li and Na systems are formally identical, sodium's larger ionic radius, slower diffusion kinetics, and distinct interfacial chemistry[63] fundamentally alter how materials behave when processed, integrated, and cycled. As a result, electrode chemistries that underpin modern LIBs have no direct sodium analogues.

Beyond our group's initial work there are a few other indications that nanoscaling works for sodium ion systems. In early research, 1D nanowires ($Na_{0.44}MnO_2$) by hydrothermal synthesis was put forward to significantly reduce diffusion path length for sodium ion transport, and also relieve the strain caused by the large volume change (~13%) during cycling[64]. These nanowire arrays, however, showed noticeable non-uniformity in both spatial distribution and structural dimensions, severely limiting capacity retention which decreased to 88% of initial value after just

20 cycles. $Na_3V_2(PO_4)_3$ (NVP) nanoparticles were synthesized and coated with a carbon layer via hydrothermal assisted sol-gel method[65]. The core-shell nanostructure guarantees good contact and relieves the strain effect during cycling, leading to capacity retention of 99.6% after 50 cycles. However, the energy density of the device is limited by low voltage of NVP (1.7 V vs. Na/Na^+) and it still relies on graphite (~10% wt) to improve electronic conductivity which reduces the effective energy. A 3D holey-carbon framework design has been reported to further improve the performance of NVP material[66]. The one-step method simultaneously produces porous carbon and NVP particles (~50 nm), with the porous carbon acting as a template that wraps the NVP to form a composite nanostructure. This three-dimensional holey-carbon framework enables a high reversible capacity of 113.9 mAh/g, approaching the theoretical limit (118 mAh/ g), with a retained capacity of 65.4 mAh g^{-1} (57.4%) after 1000 cycles. Additionally, γ'-V_2O_5 nanoparticles were also employed in SIBs, featuring a relatively homogeneous size in the range of 100-200 nm[17,67], showing a significant available capacity of 145 mAh/g and 91% capacity retention after 200 cycles.

According to the works of nanostructured sodium-ion batteries above, we can find that almost all of these works still use traditional chemical synthesis methods (e.g. hydrothermal method) to prepare nanomaterials for batteries. Although these methods are usually simple and easy to operate, the conditions of the reactions are often incompatible with semiconductor production. The precision of traditional chemical reaction techniques cannot satisfy the requirement of semiconductor production. Additionally, the integration of nanomaterials into nanoconfined environments of microbattery systems still remains to be a challenge for us. In this context, it's meaningful to find a new method to fabricate nanostructured microbatteries. We've developed an electrochemical phase engineering method to prepare γ'-V_2O_5 material via ALD process in chapter 3[68]. Planar Si wafer was employed to be the substrate for thin-film V_2O_5

electrodes which showed reversible sodiation reaction and high initial capacity (130 mAh/g). However, the 2D nanostructure cannot balance energy density and power density. The energy density would rapidly degrade if we wanted to increase the capacity by depositing thicker V_2O_5 electrode. Since 2D nanostructure doesn't work and ALD works well with 3D nanostructure, we turned to more complicated 3D nanostructure to seek for better SIBs.

Among semiconductor techniques, atomic layer deposition (ALD) is a thin-film technique with high precision that has been adopted to tackle key limitations of sodium-ion batteries (SIBs). ALD's self-limiting surface chemistry enables conformal, angstrom-to-nanometer control of coating thickness on complex, high-aspect-ratio electrodes[17,20]. This allows protective layers to be thin enough to avoid excessive mass penalty while still delivering robust interfacial control. Usually, ALD coatings in SIBs serve three complementary functions: (1) interfacial stabilization to form engineered SEI/CEI layers that suppress electrolyte decomposition, HF attack, and transition-metal dissolution; (2) mechanical buffering to accommodate or constrain volume changes to prevent particle pulverization and dendrite formation; (3) kinetic enhancement to create nanostructured surfaces or pseudocapacitive interfaces that shorten Na^+ diffusion paths[16,69]. Typical materials demonstrated in the literature include Al_2O_3, TiO_2, HfO_2, ZrO_2, Na-containing oxides, and mixed oxysulfides, applied to carbon anodes, alloy/metal anodes (Na, Sn, Ge), transition-metal oxides/sulfides, layered oxide cathodes (P2/P3/O3), NASICON-type electrodes, and thin-film solid electrolytes (e.g., NaPON)[70–73]. These examples reported tried to deposit Al_2O_3 on hard carbon and Na metal to form stable artificial SEI, TiO_2 on MoS_2 and Sn to buffer volume change, and NaPON as an ultrathin solid electrolyte. Therefore, ALD has been confirmed to be a mature semiconductor technique working for sodium-ion batteries.

ALD-deposited films improve SIB performance through chemical, mechanical, and transport mechanisms that often act together. Chemical passivation is that ultrathin alumina or oxide films react or bond with surface groups (e.g., Al–O–C formation) to suppress parasitic reactions and limit active-material dissolution. Mechanical reinforcement is that conformal shells and buffer layers reduce local strain, prevent crack propagation, and stabilize phase transitions (for example, suppressing P2-O2 or P3-O3 transitions in layered cathodes). Ionic/electronic tuning is that some ALD films (or their transformed derivatives during sodiation) can become Na-conductive or provide pseudocapacitive sites, improving interfacial Na^+ transport without blocking electron flow when optimized in thickness and composition[69].

Although laboratory studies consistently report improved initial Coulombic efficiency, reduced capacity fade, better rate capability, and longer cycle life when ALD coatings are optimized in regard to material, thickness, and deposition conditions, several challenges still remain before ALD solutions can be widely commercialized for SIBs: (1) the detailed structure–function relationships for Na systems (SEI/CEI chemistry, Na-consumption during initial sodiation, and long-term evolution) require operando characterization and multiscale modeling; (2) ALD-grown NaPON and other solid-state electrolytes currently show ionic conductivities far below commercial targets, requiring further materials innovation and interface engineering; (3) ALD's low deposition rate and high equipment/precursor costs demand process innovations (e.g. spatial ALD, roll-to-roll, plasma enhancement, etc.) and precursor recycling strategies to be economically viable at battery manufacturing scale. So far, we cannot get rid of the limitations listed above to make a perfect SIB, but ALD is still a promising technique providing a uniquely precise toolbox for engineering electrode interfaces and architectures, delivering clear lab-scale

advancements in stability and kinetics, ionic conductivity for solid electrolytes, and industrial scalability for commercialized products.

In this work, we fabricate a full battery consisting of a porous anodic aluminum oxide (AAO) template as the substrate, an array of V_2O_5 nanotubular electrodes integrated with Pt nanotubular current collectors, and liquid electrolyte in AAO nanopores. Thousands of microbatteries in parallel make up a microbattery-array within AAO substrate, and they connect to each other by Pt nanotubular current collectors covering the interval surface between nanopores. As a continuation of our previous research on synthesis method for γ'-V_2O_5, we use the same method preparing V_2O_5 electrodes but with nanotubular morphology rather than previous planar electrodes. The 3D nanopore battery shows a high capacity of 44 μAh/cm^2 (one Na ion per V_2O_5 insertion). The capacity reached 80% of initial capacity after 720 cycles in comparison with our thin-film electrode (70 cycles)[68], displaying an over tenfold improvement from 2D planar morphology to 3D nanopore framework. This is also the best capacity retention performance among SIB systems utilizing transition metal oxide electrodes to the best of our knowledge[74–76].

1.5 Goal of Dissertation

To summarize, this dissertation has 3 goals:

1. Synthesize a high power and high energy sodium ion cathode material that can be conformally coated over 3D substrates.
2. Integrate this material into nanostructured 3D substrates.
3. Understand the transport mechanisms of Na^+ ions in these nano-confined environments.

Chapter 2: Experimental Methods

2.1 Deposition Method Development

2.1.1 Substrate Preparation

In early stage of this program, the thin-film V_2O_5 was deposited on Si wafers to make planar V_2O_5 electrodes for the following research. Si wafers (thickness, 400 μm) were purchased from University Wafer, and each one was cut into square pieces (10 × 10 mm). All diced wafers were cleaned using deionized water, isopropyl alcohol (IPA), acetone, and methanol sequentially to get rid of the possible surface contamination. The cleaned Si wafers were dried in an oven for ~12 h before ALD process.

To fabricate 3D microbatteries, we chose porous anodic aluminum oxide as the substrate. Porous anodic aluminum oxide templates (AAO, thickness, 50 μm; pore diameter, 200 nm; interpore distance, 450 nm; diameter, 13 mm) were purchased from Topmembranes. The AAO templates were cleaned via ultrasonic in deionized water, IPA, acetone, and methanol for 20 min respectively. Then AAO templates were dried at 90 ℃, vacuum (3 mbar) for 12 h before ALD process.

2.1.2 Atomic Layer Deposition Process for V_2O_5

Atomic layer deposition was done using a Beneq TFS500 ALD platform. The reactor chamber was pumped down to 3 mbar before deposition. The deposition of V_2O_5 uses vanadium triisopropoxide (VTOP) and O_3 as precursors controlled by corresponding valves. VTOP was purchased from Sigma Aldrich, and O_3 was obtained by plasma of oxygen gas (Airgas UHP, 99.99%) in MKS O3MEGA™ Ozone Delivery Subsystem during the deposition. The reaction was conducted at 170 ℃. After deposition of V_2O_5 by ALD, the diced wafers were put into the

Thermolyne 79300 tube furnace to anneal at 350 ℃ for 12 h to get α-V_2O_5. More details of ALD process to prepare V_2O_5 have been summarized by previous work of our group[53].

2.1.3 Sputtering Process Development

An AJA ATC 1800 Sputtering unit was utilized to deposit Ti and Pt on Si wafers or AAO substrates. The main chamber was pumped to a base pressure (⩽5 mTorr) before introducing process gas.

Deposition of Ti adhesion layer: Flow Ar gas to achieve a working pressure of 3–5 mTorr (typical range for magnetron sputtering). Choose DC sputtering mode for Ti deposition. Typical power is 150W on a 3″ target to obtain moderate deposition rates. Rotate substrate at 10 rpm for uniformity of deposition. Keep substrates at room temperature. Calibrate deposition rate with the QCM prior to the run to precisely control the thickness. Typical Ti deposition rates for these conditions are on the order of 0.5–2 Å/s. 50 nm Ti was deposited as an adhesion layer to connect Si substrates and Pt layer.

Deposition of Pt layer: After Ti deposition, allow the chamber to stabilize; optionally perform a short (2 min) Ar purge and recondition the Pt target with shutter closed for 5 min. Maintain the pressure at 3 mTorr. Use DC sputtering for Pt and setup the power at 150W on a 3″ Pt target. Pt has lower sputter yield so lower rate is expected than Ti. Continue substrate rotation similar to the deposition of Ti layer and maintain the room temperature. Calibrate Pt deposition rate with QCM to precisely control the thickness of Pt layer. Typical Pt deposition rate under these conditions is in the range of 0.5–2 Å/s depending on power and source geometry. 100 nm Pt was deposited on Si substrates and 30 nm Pt was deposited on AAO substrates.

2.2 Synthesis of γ'-V_2O_5

2.2.1 Preparation of Thin-Film V_2O_5 Electrodes

Diced Si wafers were RCA cleaned and subsequently thermally oxidized in a Tystar CVD system to form a 400 nm SiO_2 layer. A 50 nm Ti layer and a 100 nm Pt layer were deposited sequentially via AJA ATC, respectively. V_2O_5 was deposited next by a Beneq TFS500 ALD reactor. The precursor was vanadium triisopropoxide (VTOP) which reacted with O_3 at 170 ℃ using optimized conditions as discussed in ***2.1.1***. After deposition, the diced wafers were put into a Thermolyne 79300 tube furnace and annealed at 350 ℃ (exposed to air) for 12 h to obtain α-V_2O_5. Next it was lithiated via galvanostatic electrochemical insertion in a beaker cell which also contained 1 M $LiClO_4$ in propylene carbonate (PC) as the electrolyte and Li metal counter electrode. The lithiation process was deployed at 1/10 C-rate, and the potential was held at cutoff voltage of 2.6 V (vs. Li/Li^+) for 5 h. δ-LiV_2O_5 electrode was obtained after lithiation, then it was returned to the Beneq TFS500 ALD reactor and annealed at 250 ℃ for 3 h under vacuum to get γ-LiV_2O_5. Galvanostatic electrochemical delithiation was in a home-made beaker cell. γ-LiV_2O_5 electrode was delithiated at 1/10 C and the potential was held at cutoff voltage of 3.8 V (vs. Li/Li^+) for 5 h to finally achieve a γ'-V_2O_5 electrode.

2.2.2 Preparation of 3D Structured V_2O_5 Electrodes

AAO is the template for the following deposition. Pt was chosen as the current collectors due to its high electrical conductivity (9.43×10^6 S/m) and electrochemical inertness. The Pt layer (thickness, 25 nm) was deposited via an AJA ATC 1800 Sputtering unit using the same recipe. The V_2O_5 layer was deposited on the substrate by a Beneq TFS500 ALD device using a previously published process [53,68]. Details of the ALD process can be found in the previous section 2.1.2. The sample was then annealed in a Thermolyne 79300 tube furnace at 350 ℃ in air for 12 h to get

crystalline α-V_2O_5. The α-V_2O_5 electrodes were lithiated via galvanostatic electrochemical insertion in a self-made beaker cell which also contains 1 M $LiClO_4$ in PC as electrolyte and a Li metal counter electrode. The charge rate was 1/10 C, and the cutoff voltage was 2.6 V (vs. Li/Li^+). The sample was put in Beneq TFS500 ALD device to be annealed at 350 ℃, under vacuum for 3 h to convert δ- LiV_2O_5 to γ-LiV_2O_5. Finally, as in the planar case, it was put back to home-made beaker cell to go through Galvanostatic electrochemical deinsertion at 1/10 C (cutoff voltage, 3.8 V) to produce γ'-V_2O_5.

2.3 Structural Characterization

To trace the evolution of crystalline structure throughout the synthesis route preparing thin-film γ'-V_2O_5, multimodal spectroscopic analysis including Raman Spectroscopy and X-ray diffraction spectroscopy (XRD) was conducted. Additional physical inspection was conducted through cross-sectional scanning electron microscopy (SEM).

2.3.1 Sample Preparation

The synthesis route to prepare γ'-V_2O_5 thin film includes steps of annealing, lithiation, cleaning, 2nd annealing, and delithiation. The samples corresponding to each step were characterized by the following techniques to trace the evolution of crystalline of V_2O_5 materials during the synthesis.

2.3.2 Raman Spectrum

The Raman spectrum was measured with the HORIBA's LabRam Jobin Yvon confocal Raman microscope. The excitation source was He:Ne laser (532 nm). A 100× objective was used to focus the laser on samples to a spot. Since γ'-V_2O_5 would anneal at high temperature, the laser

filter was set to D2, and the exposure time was 60 s. Three points of each sample were recorded to assure reliability of Raman spectra.

2.3.3 X-Ray Diffraction

Grazing incidence X-ray diffraction

Grazing incidence X-ray diffraction (GI-XRD) measurements were conducted using a high-resolution Rigaku SmartLab diffractometer equipped with a 9 kW Cu Kα rotating anode X-ray source (λ = 1.5406 Å). This surface-sensitive technique was employed to investigate the crystalline structure of thin films deposited on silicon substrates while effectively minimizing the diffraction contribution from the underlying substrate. The film-coated silicon wafer was mounted flat on the sample stage, with the film surface oriented upward. Precise sample alignment was achieved using the built-in optical alignment system of the instrument. The measurements were performed in grazing incidence mode with the incident angle (ω) set to 0.50°, which corresponds closely to the critical angle for X-rays on silicon. This angle was chosen based on literature evidence indicating that ω = 0.50° effectively suppresses substrate diffraction while maximizing surface sensitivity. To further enhance the data quality and surface sensitivity, an additional scan was performed at ω = 0.55° (i.e., critical angle + 0.05°). XRD patterns were recorded over a 2θ range of 10° to 70. A step size of 0.05° and a scan rate of 0.025° per second were employed to ensure high angular resolution and optimal counting statistics. The diffractometer was operated in parallel beam geometry using appropriate Soller slits and divergence controls to optimize peak resolution and reduce background noise. Receiving slits and a monochromator were employed as necessary to further improve the signal-to-noise ratio. Data acquisition and analysis were carried out using the SmartLab Studio II software package. This GI-XRD setup enabled precise and

reliable characterization of the crystalline phases present in the thin film while minimizing interference from the silicon substrate.

X-ray Reflectivity (XRR)

X-ray reflectivity (XRR) measurements were performed using the Rigaku SmartLab high-resolution diffractometer, equipped with a 9 kW Cu Kα X-ray source (λ = 1.5406 Å), to determine the thickness, density, and surface/interface roughness of the thin films deposited on silicon wafers. The measurement was carried out in a specular reflection geometry, where the incident and reflected angles (ω and 2θ) are equal, enabling sensitive probing of electron density contrast along the surface normal. Prior to measurement, the system was allowed to thermally stabilize, and the sample was carefully mounted on a high-precision goniometer (five-axis high-resolution) stage, ensuring a flat and uniform film surface aligned with the X-ray beam. A preliminary alignment scan was conducted to optimize the incident angle and ensure accurate detection of the reflected beam. The reflectivity profile was collected over a 2θ range of 0.05° to 5° to capture the critical angle and interference fringes (Kiessig fringes) indicative of film thickness and interface quality. The scan was performed in continuous mode with a step size of 0.003° and a counting time of 2 seconds per step until the reflectivity curve approached a flat baseline for more accurate modeling during data fitting. Data acquisition and control were managed using the SmartLab Studio II software suite.

2.3.4 Microscopy

Scanning Electron Microscopy (SEM) was performed on a dual-beam field emission SEM system (Tescan, XEIA3) with a 10 kV acceleration voltage and a Hitachi SU-70 Schottky field emission gun scanning electron microscope with a 10 kV acceleration voltage. Both devices have

already been integrated with Energy-Dispersive X-ray Spectroscopy (EDS) for characterizing distribution of target elements.

2.4 Electrochemical Measurements

The electrochemical measurements for thin-film V_2O_5 electrodes were madeed using a custom beaker cell. Later work on more complicated nanostructured V_2O_5 electrodes relies on T-cell electrochemical test platform which will be introduced in following sections.

2.4.1 Electrochemical Measurements of Planar V_2O_5 Electrodes

Electrochemical tests were performed at room temperature in custom two-electrode galvanic cells which have V_2O_5 working electrodes and lithium or sodium metal counter electrodes as shown in Figure 3.7. The electrolyte is a solution 1 M $LiClO_4$ in propylene carbonate (PC) or 1 M $NaClO_4$ in PC/ethylene carbonate (EC) (1:1). All galvanic cells were assembled in a glovebox filled with argon in which the oxygen and moisture level were kept under 1 ppm. All electrochemical tests were finished under the argon atmosphere in the glovebox, and the measurements were controlled by Biologic VSP potentiostat.

2.4.2 Electrochemical Measurements of 3D Structured V_2O_5 Electrodes

Porous anodic aluminum oxide templates (thickness, 50 μm; pore diameter, 200 nm; interpore distance, 450 nm; diameter, 13 mm) were purchased from Topmembranes. The AAO templates were cleaned via ultrasonic in IPA (isopropanol), acetone, methanol, deionized water, for 20 min respectively. Then AAO templates were dried at 90 ℃, vacuum overnight (3 mbar) for 12 hours. Pt was chosen as the current collector due to high electrical conductivity and electrochemical inertness. The Pt layer (thickness, 25 nm) was deposited via an AJA ATC 1800

Sputtering unit. The electrode V_2O_5 layer was deposited on the substrate by a Beneq TFS500 ALD using a previously published process which is briefly summarized here. Vanadium triisopropoxide (VTOP) was reacted with O_3 at 170 °C using previously optimized conditions. After deposition of V_2O_5 the 3D electrodes were annealed in a Thermolyne 79300 tube furnace at 350 °C in air for 12 h to crystallize to α-V_2O_5. This phase was then converted to γ'-V_2O_5 using a previously published recipe which is briefly outlined here[53]. The electrodes were then lithiated via galvanostatic electrochemical insertion in 1 M $LiClO_4$/propylene carbonate (PC) with a Li metal counter electrode at 1/10 C-rate, and a cutoff voltage of 2.6 V vs. Li/Li^+ to achieve δ-LiV_2O_5. The sample was then annealed a second time at 350 °C for 3 h under vacuum. Finally, the annealed film is galvanostatically de-lithiated at 1/10 C-rate to get the γ'-V_2O_5 phase. The configuration of the nanopore battery based on AAO template is shown in Figure 4.1.

In an argon-filled glovebox, custom three-electrode test platforms were formed by modifying standard 1/2" PFA swaglock union-T tube fitting. The inner diameter was drilled to a diameter of 1/2 inch to accommodate the nanopore electrodes. Customized ½-inch diameter stainless steel rods were used to hold the nanopore and Na metal electrodes at a fixed distance (36 mm) and to make external electrical contact. The inner volume of Swaglok T-cell was filled with 1 M $NaClO_4$ in PC/EC (5 mL). Each cell is composed of two AAO nanopore electrode arrays and a. Na metal electrode as reference. The configuration of the T-cell is shown in Figure 4.1.

In addition to the T-cell, a beaker cell which has same layout as section *2.4.2* was assembled as a control group. It has the configuration of γ'-V_2O_5 (working electrode) vs. Na (counter electrode) and the same electrolyte as T-cell (1 M $NaClO_4$ in PC/EC). All components of the battery were integrated into a 100 mL beaker, as shown in Figure 3.7.

$NaClO_4$ and propylene carbonate (PC) were purchased from Sigma Aldrich. Ethylene carbonate (EC) was purchased from LANDT and used as received. $NaClO_4$ was dried at 140 ℃ for 24 h under vacuum (3 mbar) before electrolyte preparation. Na cubes were purchased from Sigma Aldrich and were diced into foil. The electrolyte was 1 M $NaClO_4$ in PC/EC (1:1 by volume). A three-electrode T-cell was used for electrochemical testing of the symmetric nanopore sodium ion battery. During the presodiation process, two V_2O_5 electrodes were simultaneously connected to the potentiostat as working electrodes, while the Na metal electrode was connected to potentiostat as a counter electrode. The connection of three-electrode T-cell to potentiostat for presodiation is shown in Figure 4.3. The T-cell discharged at 1/10 C until the output voltage reached 3.1 V, and held the voltage at 3.1 V for 5 h to make sure both V_2O_5 electrodes were half-sodiated to $Na_{0.5}V_2O_5$. For the following electrochemical characterization, the T-cell was reconnected as a three-electrode system. Each of the V_2O_5 electrodes were separated as the working electrode and the counter electrode respectively, and Na metal electrode as the reference electrode. The three-electrode system deconvolutes the cell voltage and provides information on working and counter electrodes simultaneously. All galvanic cells were assembled in a glovebox filled with argon in which the oxygen and moisture level were kept under 1 ppm. All electrochemical tests were controlled by Biologic VSP potentiostat.

Chapter 3: Electrochemical Phase Engineering of γ'-V_2O_5 Thin Films for Sodium-Ion Storage Electrodes

3.1 Chapter Summary

This chapter tells the development of an electrochemical phase engineering method to synthesize γ'-V_2O_5 thin films for sodium-ion storage electrodes. These results were published in ACS Omega (2025) titled "*Electrochemical Phase Engineering of γ'-V_2O_5 Thin Films for Sodium-Ion Storage Electrodes*. ACS omega 10 (50), 61414-61421".

As discussed in the introduction, V_2O_5 is a promising sodium ion cathode material due to its high theoretical capacity (147 mAh/g) and working voltage (3.3 V vs. Na/Na^+). Among its various crystal phases, γ'-V_2O_5 has large interlayer spacing ensuring the reversible insertion-extraction of sodium ions. However, current synthesis methods for γ'-V_2O_5 require high temperatures (>600 ℃) and toxic chemicals (NO_2BF_4) which make the preparation demanding. Herein, we put forward an electrochemical phase engineering method combining thermal annealing and electrochemistry to easily prepare thin-film γ'-V_2O_5. Electrochemical characterization shows near ideal performance as a thin film cathode material for sodium ion batteries, with high initial capacity (140 mAh/g), high working voltage (3.3 V), and exceptional coulombic efficiency (>98%). The γ'-V_2O_5 thin film has electrochemical performance similar to γ'-V_2O_5 powder, indicating thin-film morphology of γ'-V_2O_5 also works for sodium ion batteries.

3.2 Phase Engineering towards γ'-V_2O_5 Thin Film Electrode Material

3.2.1 Synthesis Route to Prepare γ'-V_2O_5 Thin Film Electrodes

To improve the sodiation of vanadium-oxide based electrode systems, a new synthesis route to γ'-V_2O_5 was developed. A summary of this method is shown in Figure 3.1. The method consists of a hybrid combination of electrochemical lithiation and thermal annealing to produce stable thin-films of γ'-V_2O_5. First, thin-films of α-V_2O_5 are produced via atomic layer deposition, as shown in step A. These films are then annealed in air at 400 C for 3 h, ensuring fully crystalline and uniform α-V_2O_5, and the characteristics of the film agree well with standard literature practice[22]. After the initial annealing step, the films are placed as working electrodes into a two-electrode beaker cell with 1M $LiClO_4$ in PC/EC as the electrolyte, and lithium metal as the counter/reference electrode. These cells have open circuit voltages (OCV) of 3.5 V and then discharge to 2.6 V at 0.1C to get one-lithium-insertion into the unit cell of V_2O_5 crystal structure[77]. This lithiated-phase is known as δ-LiV_2O_5[22]. While in δ phase the samples are annealed for a second time at 250 ºC for 3 h under vacuum (3 mbar) to form γ-LiV_2O_5. Finally, the films are returned to the electrochemical cell used above and the lithium is removed by electrochemistry at 0.1C forming the γ'-V_2O_5, an ideal structure for sodiation due to its wider crystal unit cell[50].

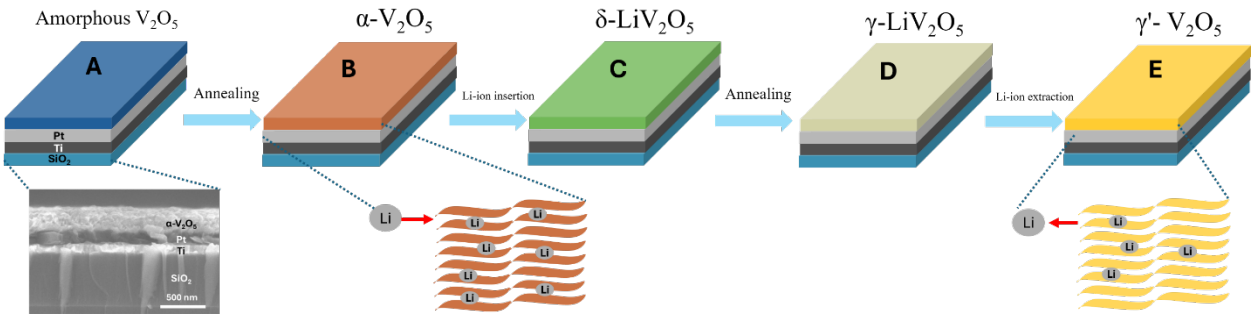

Figure 3.1. Synthesis route of γ'-V_2O_5. The method combines electrochemical lithiation and thermal annealing. Electrochemical lithiation and delithiation were done in two-electrode beaker cell. The substrate remained stable during the synthesis. V_2O_5 layer undergoes phase transitions from α-V_2O_5 to γ'-V_2O_5.

Since the synthesis route includes electrochemical lithiation and delithiation steps, the electrochemistry results were used to understand the phase-transition process during preparation

of γ'-V_2O_5 are shown in Figure 3.2. The lithiation curve has two plateaus at 3.4 and 3.2 V respectively, which correspond to phase transition from α-V_2O_5 to ε-$Li_{0.5}V_2O_5$ and ε-$Li_{0.5}V_2O_5$ to δ-LiV_2O_5 respectively (Figure 3.2, black curve). As witnessed in Figure 3.2, the electrodes were held at 2.6 V vs Li/Li^+ and 3.8 V vs Li/Li^+ to ensure full lithiation and delithiation of the electrodes via electrochemical polarization effect[22]. The currents were monitored, see Figure 3.3, and held to allow the current decay to a minimum. Usually, it takes over 5 hours to let the current decay to almost zero which means almost complete lithiation or delithiation. The additional 10% capacity relative to the theoretical value (147 mAh/g) witnessed is assumed to be combination of the additional surface area provided by the thin-film nature of the material, electrochemical polarization of the electrode, and potential side reactions due to the carbonate electrolyte[78,79]. These results are consistent with the literature[22], and confirm the crystallinity of α-V_2O_5 at one-lithium insertion to produce δ-LiV_2O_5. The delithiation curve after the 2nd annealing (step D, Figure 3.1) displays plateaus at 3.6 and 3.5 V, as shown in Figure 3.2 (blue line) which represent one-lithium deinsertion to form γ'-V_2O_5. Ideally, γ'-V_2O_5 can be obtained to be cathode material of sodium ion batteries after delithiation process for the following characterizations and electrochemical measurements.

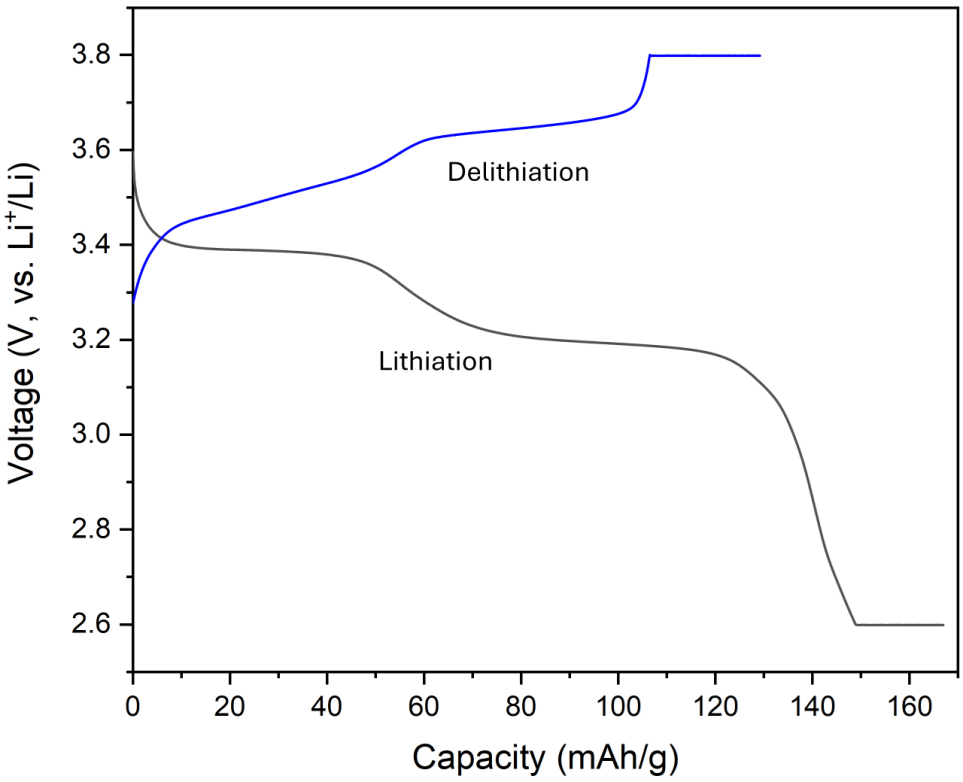

Figure 3.2. Lithiation (black line) and delithiation (blue line) curves of synthesis route. Curve a corresponds to the discharging step at 1/10 C was done to produce δ-LiV_2O_5 by one-lithium insertion reaction. In curve b, the two-electrode beaker cell charged at 1/10 C to delithiation γ-LiV_2O_5 to get γ'-V_2O_5.

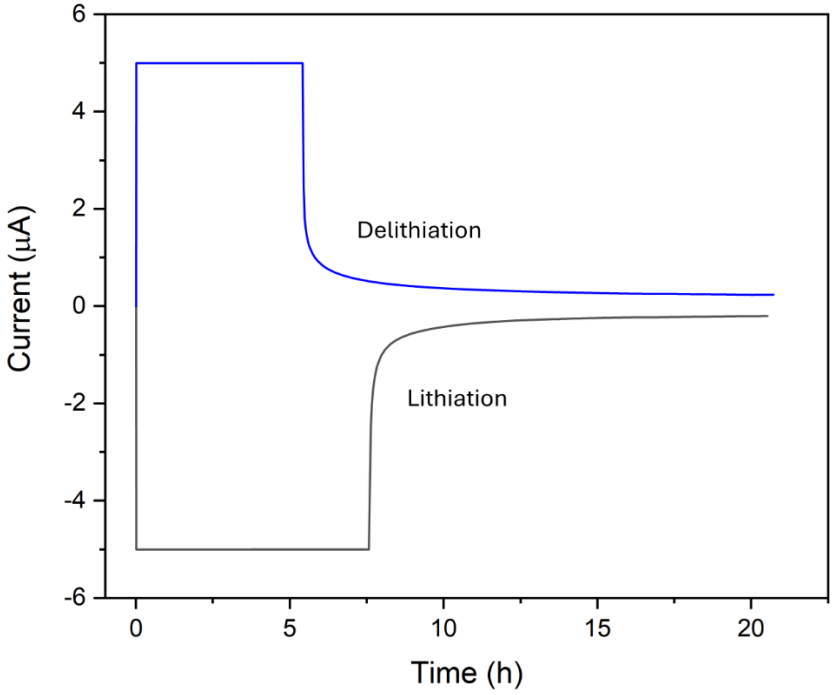

Figure 3.3. Electrochemical lithiation-delithiation of V_2O_5 in γ'-V_2O_5 Synthesis Route. Constant current was applied to lithiation and delithiation of V_2O_5 before and after thermal annealing respectively. Holding the voltage after constant current caused the current gradually decreased to a low level approaching zero current, which ensured the complete lithiation and delithiation.

3.2.2 Metrology of Thin-Film γ'-V_2O_5 Electrodes

To confirm the evolution of crystalline phase throughout the electrochemical phase engineering process outlined in **Figure 3.1**, multimodal spectroscopic analysis was conducted through Raman Spectroscopy and X-ray diffraction spectroscopy (XRD). Additional physical inspection was conducted through cross-sectional scanning electron microscopy (SEM).

Raman Spectrometry

To determine the local bonding environment of the vanadium (V) and oxygen (O) atoms in the thin film V_2O_5 throught out the electrochemical phase engineering process, we used Raman spectroscopy ranging from 50 cm^{-1} to 1200 cm^{-1}, with the results shown in Figure 3.4. Raman spectra of the materials at each step during the synthesis were collected to explore the change in bonding environment and compare to known crystal structures. The vanadium-oxygen (V-O) bond distance varies with phase evolution. Therefore, tracking the evolution of characteristic peaks throughout our synthesis method would be a clear indication of variation in crystal structures.

Step 1. α-V_2O_5: The as deposited V_2O_5 is amorphous and annealed at 400 ℃ for 3 h to form α-V_2O_5. The spectrum (Figure 3.4, black line) has characteristic peaks at 995 cm^{-1}, 700 cm^{-1}, 525 cm^{-1}, 480 cm^{-1}, 405 cm^{-1}, 305 cm^{-1}, 285 cm^{-1}, 195 cm^{-1}, and 145 cm^{-1} respectively. The peaks above 480 cm^{-1} are indicative of bond-stretching vibrations while the peaks below 480 cm^{-1} correspond to bond-bending vibrations. The peak pattern is consistent with theoretical Raman-active modes of α-V_2O_5, demonstrating α-phase of V_2O_5 after annealing.

Step 2. δ-LiV_2O_5: After one-lithium insertion, δ-LiV_2O_5 is expected (Figure 3.4, red line). The spectrum shows an obvious peak evolution compared with α-V_2O_5. The intense peak at 143 cm^{-1} disappears and a shift from 995 cm^{-1} to 965 cm^{-1} is seen. A shoulder at 982 cm^{-1} appears on the right of 965 cm^{-1}, suggesting the multiple V-O stretching modes caused by lithium insertion[80], which confirms that δ-LiV_2O_5 is obtained after lithiation.

Step 3. γ-LiV_2O_5: The 2nd annealing after lithiation enables a phase-transition from δ-LiV_2O_5 to γ-LiV_2O_5. The characteristic peak at 971 cm^{-1} and a shoulder at 990 cm^{-1} are observed in V-O stretching mode region[81]. Other peaks at 149, 173, 222, 297 and 329 cm^{-1} appear similar to γ-LiV_2O_5 previously reported in literature[82].

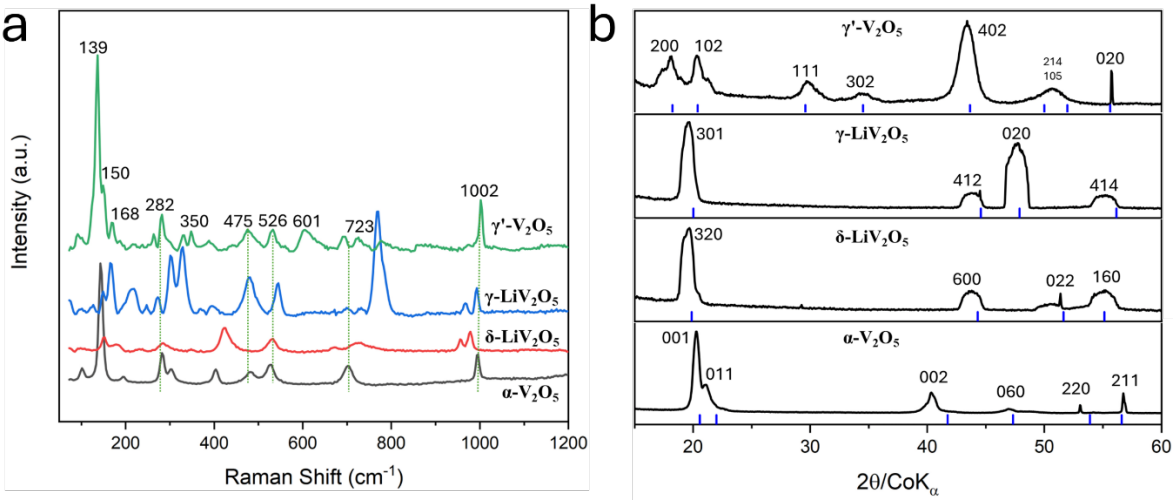

Figure 3.4. (a) Raman spectra of V_2O_5 materials at each step of synthesis route. The curves include α-V_2O_5, δ-LiV_2O_5, γ-LiV_2O_5, and γ-V_2O_5. (b) XRD spectra of V_2O_5 materials at each step of synthesis route. The curves include α-V_2O_5, δ-LiV_2O_5, γ-LiV_2O_5, and γ-V_2O_5.

Step 4. γ-LiV_2O_5: Finally, γ-LiV_2O_5 is electrochemically delithiated to produce γ'-V_2O_5 (Figure 3.4a, green line) the desired phase. The highest frequency peak at 1002 cm^{-1} is caused by asymmetric stretching modes of V=O bonds[49]. The peaks at 723 and 601 cm^{-1} correspond to asymmetric and symmetric stretching modes of V-O-V bridges. The peak at 526 cm^{-1} is related to

asymmetric stretching modes of V-O bonds. More peaks at 139, 168, 282 and 359 cm^{-1} are assigned to the complicated distortion of layered structure of γ'-V_2O_5[83]. The peak at 792 cm^{-1} which does not match any characteristic peak of γ-LiV_2O_5 may be from Li_3VO_4 generated during thermal annealing[54].

The peak patterns in **Figure 3.4a** confirm the phase transition from α-V_2O_5 to δ-LiV_2O_5. As mentioned, the Raman-peak pattern is strongly affected by lithium-insertion into the V_2O_5 host lattice. The introduction of Li-O bonds increases the degree of disorder and puckering of crystal structure which results in decreasing peak intensity for in-phase rotation of V-O framework and out of plane V=O symmetric bond-stretching[84]. The phase-transition from δ-LiV_2O_5 to γ-LiV_2O_5 is finished in the 2nd annealing process. More characteristic peaks emerge in the spectrum and some previous peaks shift in contrast to δ-LiV_2O_5. In the last step of the synthesis route, γ'-V_2O_5 is produced through electrochemical delithiation of γ-LiV_2O_5. The elimination of lithium ions in V_2O_5 removes the Li-O bonds and thus decreases the extent of disorder and puckering of crystal structure. This is observed through the sharpening of the Raman peaks (i.e. smaller FWHM). It can be observed that V_2O_5 does not go back to the original α-phase after the delithiation step, and the generated γ'-V_2O_5 shows a quite different Raman spectrum which means new V-O bonding environments were formed.

X-Ray Diffraction (XRD) Spectrometry

Complimentary confirmation of material phase and crystal structure was acquired through XRD. Since the samples in this work are thin films rather than bulk powders, grazing incidence XRD (0.5°) was used to increase signal intensity and avoid substrate signal. The XRD spectra of α-V_2O_5, δ-LiV_2O_5, γ-LiV_2O_5 and γ'-V_2O_5 are displayed in Figure 3b. The spectrum of α-V_2O_5 exhibits the characteristics of *hkl* reflections matching an orthorhombic crystal structure (Pmmn

space group, ICSD PDF calc. 01-090-8354)[85] which has unit cell parameters $a = 11.52$ Å, $b = 3.56$ Å, $c = 4.32$ Å[86]. Lithium-insertion distorts the crystal structure of α-V_2O_5, leading to the evolution of peak pattern from α-V_2O_5 to δ-LiV_2O_5 (Pmn21 space group, ICSD PDF calc. 01-089-8319)[87]. The 2nd thermal annealing at 250 ℃ transforms δ-LiV_2O_5 into γ-LiV_2O_5 which has a similar peak pattern but with a new *hkl* line (020) at 47.8° (Pnma space group, ICSD PDF calc. 01-070-2476)[88]. The as-synthesized γ'-V_2O_5 after delithiation of γ-LiV_2O_5 shows an orthorhombic crystal structure (Pnma space group, ICSD PDF calc. 01-090-7484)[89] which has unit cell parameters $a = 9.94$ Å, $b = 3.58$ Å, $c = 10.04$ Å, indicating a larger space than α-V_2O_5 to contain sodium ions. The combination of Raman spectroscopy, XRD spectroscopy confirms the phase transformation from α-V_2O_5 to γ'-V_2O_5 outlined in Figure 3.4. Slight variations in peak position and intensity ratios are due to the thin-film nature of the material, limiting X-ray cross-section, and available reflections[90]. We also note that the limited angle used for grazing incidence leads to lower intensities, changes in peak ratios, and some absent or shifted indices/reflections in comparison with the standard powder pattern from ICSD database. Overall, the combination of Raman and XRD provide convincing evidence of the claimed phase evolution.

Microscopy

To complete the analysis of our synthesis method and to determine more exacting thickness measurements, which will be important to electrochemical methods discussed below, cross-sectional SEM images were taken. Images of the cross-section at each stage of our proposed synthesis method including α-V_2O_5, δ-LiV_2O_5, γ-LiV_2O_5 and γ'-V_2O_5 are shown in Figure 4a-d. The thin-film structure of the samples is clearly witnessed, and the thickness of all layers were as expected. Figure 4a shows the cross-section of the α-V_2O_5, which measures a thickness of ~205 nm, as expected. After the film is lithiated from α-V_2O_5 to δ-LiV_2O_5 the film thickness increases

by ~25% (Figure 4b). After annealing, the γ-LiV_2O_5 layer (Figure 4c) still has thickness of ~250 nm, and morphology remains uniform. The desired material phase γ'-V_2O_5 is obtained by delithiation of the γ-LiV_2O_5 phase, and shows a reduced thickness of ~210 nm (Figure 4d). In general, the evolution of material phase and thin-film structure coincides well with the proposed phase changes and resulting crystal structures during synthesis. The overall volume expansion from α-V_2O_5 to γ'-V_2O_5 is only ~5%.

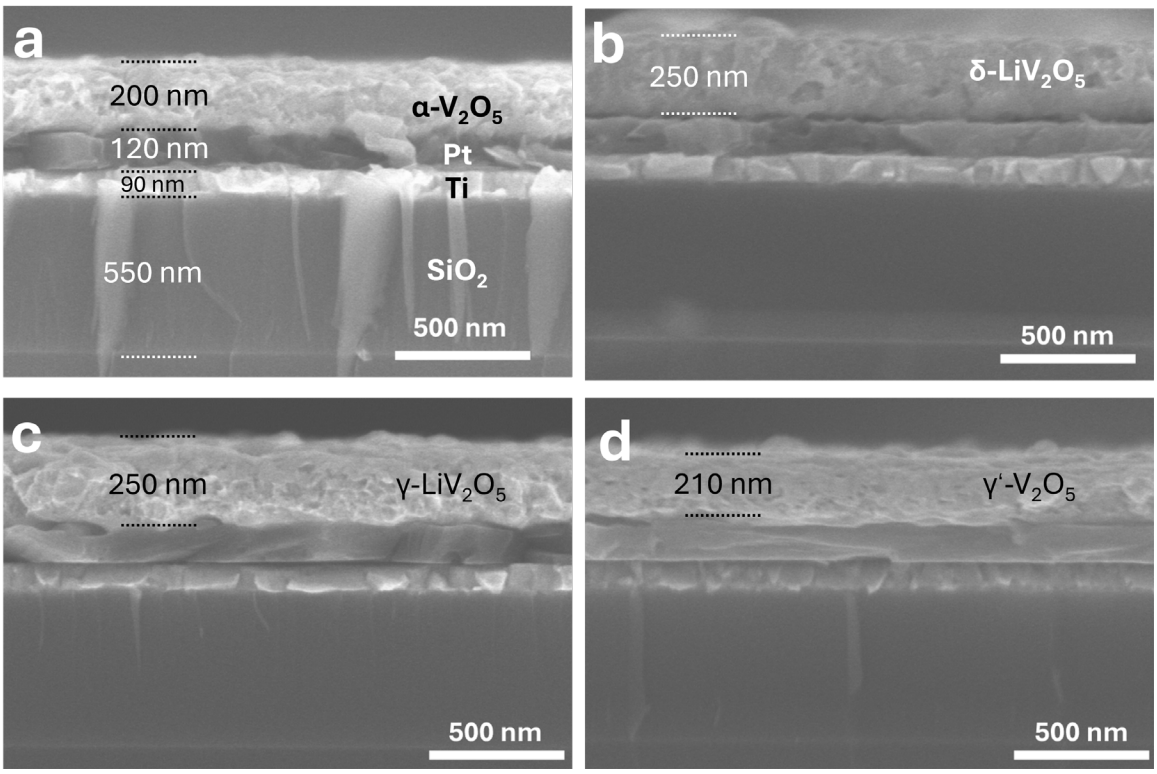

Figure 3.5. SEM images showing the layered structure of thin-film V_2O_5 electrode at each step of synthesis route. The phase evolution includes **a)** α-V_2O_5, **b)** δ-LiV_2O_5, **c)** γ-LiV_2O_5, and **d)** γ-V_2O_5. The obvious change of the thickness of V_2O_5 layer can be seen during the synthesis route.

The combination of these three metrology techniques confirms the synthesis process and intermediate material phases. Raman spectroscopy and XRD provide complementary information on the evolution of the local bonding and crystal structure. SEM images measured the volume evolution of thin-film V_2O_5 material and showed evidence of lithiation and delithiation occurring

during synthesis through changes in film thickness and therefore electrode volume. All of these data are consistent with γ'-V_2O_5 and general V_2O_5 lithiation/delithiation reported in literature.

Electrochemical Lithiation of γ'-V_2O_5

Although our focus in this chapter is synthesis of γ'-V_2O_5 for sodium-ion storage, electrochemical lithiation of γ'-V_2O_5 can help us characterize γ'-V_2O_5 material to reconfirm the crystal phase of synthesized thin-film material in comparison with literature[49,83]. Additionally, the following electrochemical measurements of γ'-V_2O_5 thin-film electrodes provide reference for us to be compared with sodiation result in later section, which would deepen our understanding on sodiation kinetics at γ'-V_2O_5 electrodes.

In order to characterize lithium insertion/deinsertion reaction in γ'-V_2O_5, charge-discharge cycles were employed. The one-lithium insertion at 1/10 C rate shows a high specific capacity of 145 mAh/g (Fig. 3.6a). The discharge curve has phase transition plateaus at 3.64 V and 3.5 V (vs. Li^+/Li) which are consistent with literature[91]. The electrochemical window of cyclic voltammograms (CVs) is 2.6-3.8 V (vs. Li^+/Li) (Fig. 3.6b). The two sets of redox peaks at 3.63 V and 3.48 V in CVs further confirm the insertion of lithium ions into V_2O_5, which match the plateaus in Fig. 3.6a. The symmetric redox peaks and the tiny peak shift with increasing scan rate indicate the reversibility of Li insertion/deinsertion reaction in γ'-V_2O_5. The γ'-V_2O_5 cathode still shows a high specific capacity at low charge-discharge rate, but it decreases with the increasing C rate (Fig. 3.6c). The specific capacity is 143 mAh/g at 0.2 C, 107 mAh/g at 0.5 C, 82 mAh/g at 1 C and 68 mAh/g at 2 C. The plateaus of charge-discharge curves at different C rates indicate that Li ion insertion reaction always exists. The γ'-V_2O_5 cathode has 80% of its initial capacity after 70 cycles when cycling at 1 C (Fig. 3.6d).

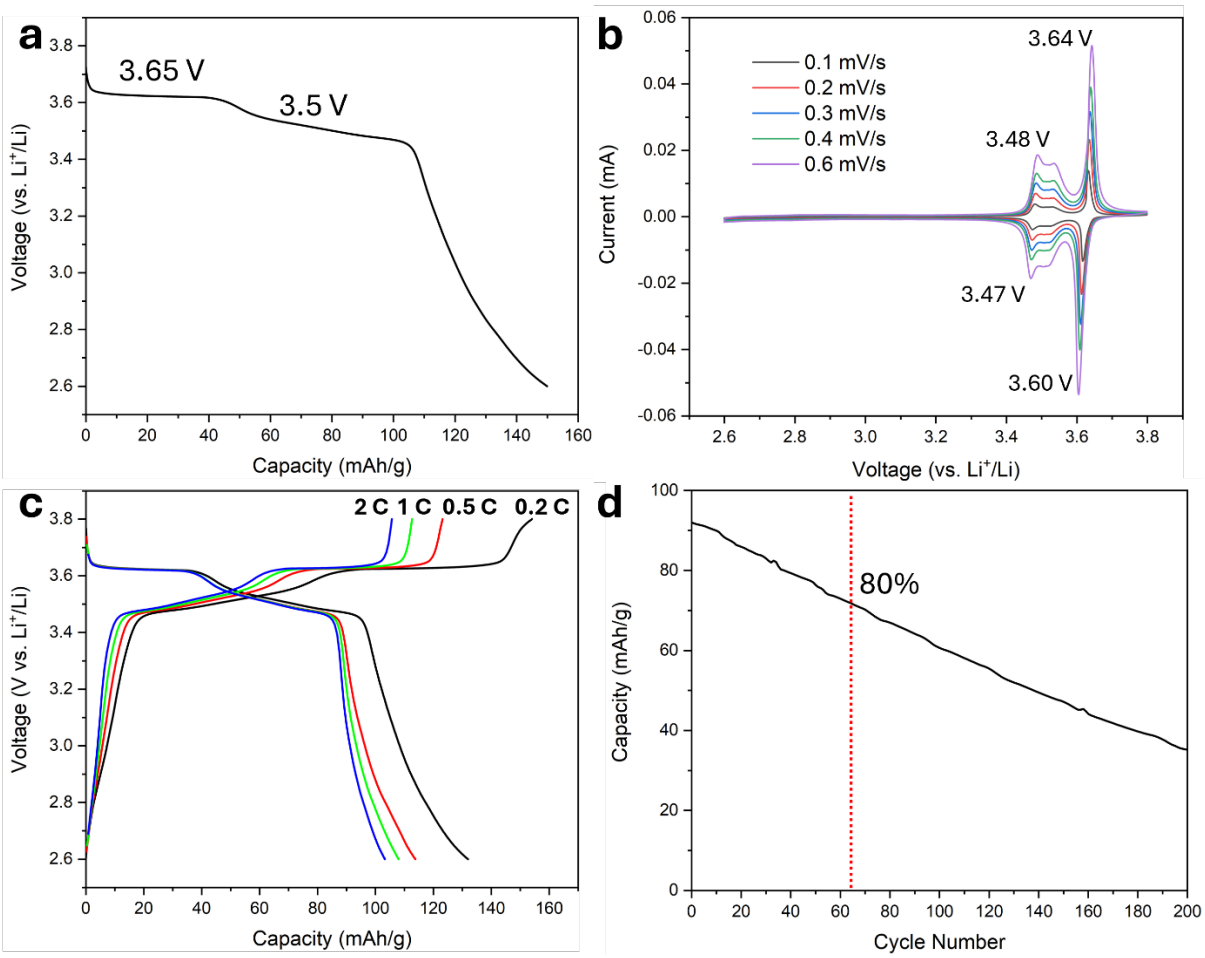

Figure 3.6. Electrochemical charge-discharge of γ'-V_2O_5/Li half-cell device. a) Galvanostatic Li ion insertion at C/10 rate with one Li ion insertion (done), and the red dash line represents theoretical capacity. b) CV of γ'-V_2O_5 cathode at different scan rates (done). c) Rate performance of γ'-V_2O_5 at different C-rate. d) Capacity retention of γ'-V_2O_5.

3.3 γ'-V_2O_5 Thin Film Electrode Material for Sodium-Ion Storage

The sodiation of γ'-V_2O_5 was measured in beaker cells as shown in Figure 3.7 (V_2O_5 vs. Na) using a solution of 1 M $NaClO_4$ in PC/EC (1:1) as the electrolyte, with the results shown in Figure 3.8a-d. Figure 3.8a shows one-sodium insertion between 3.4-1.7 V vs. Na/Na^+ at 0.1 C, and measures a specific capacity of 152 mAh/g which is ~3% higher than theoretical capacity (147 mAh/g). The additional capacity witnessed in the first cycle is attributed to the thin-film nature of

the material, pseudo capacitance, and potential side-reactions. The discharge curve has phase-transition plateaus at 3.3 V and 2.5 V (vs. Na/Na^+), comparable to values found in the literature[19]. CVs of γ'-V_2O_5 were conducted as a function of scan rate (0.1, 0.2, 0.3, 0.4 and 0.6 mV/s) with the results shown Figure 3.8b. The distribution of redox peaks is symmetric and demonstrates good reversibility of sodium insertion/deinsertion in γ'-V_2O_5. These curves show sharp de-sodiation peaks at 3.4-3.5 V and sodiation at 3.2 V, and additionally show minimal shift as a function of rate, for example, the reduction peak shifts from 3.29 V to 3.24 V when the scan rate increases from 0.1 mV/s to 0.6 mV/s, further establishing the stability of this material during sodiation. The rate dependence of the capacity is shown in Figure 3.8c. The specific capacity of γ'-V_2O_5 decreases with the increasing C rate from 140 mAh/g at 0.2 C, 98 mAh/g at 0.5 C, 81 mAh/g at 1 C, and 70 mAh/g at 2 C. Capacity retention was measured at 1C with the results shown in Figure 3.8d. These results show that γ'-V_2O_5 retains 80% of its initial capacity after 80 cycles. Therefore, γ'-V_2O_5 has much better ability for sodium storage in comparison with α-V_2O_5 as shown in Figure 3.9a-d.

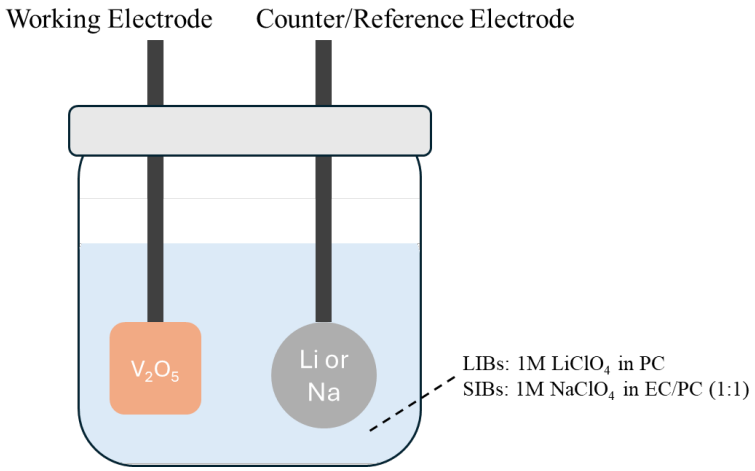

Figure 3.7. Schematic configuration of the beaker cell. All electrochemical measurements were finished using self-made beaker cell. The counter/reference electrode is Li metal and the electrolyte is 1M $LiClO_4$ in PC during lithiation and delithiation in the synthesis route. The counter/reference electrode is Li metal and the electrolyte is 1M $NaClO_4$ in EC/PC (1:1) during the test of sodiation performance.

As a control, the sodiation of α-V_2O_5 was measured in a two-electrode beaker cell with a sodium metal counter electrode in a solution of 1 M $NaClO_4$ in PC/EC as the electrolyte. The discharge curve for one-sodium ion (3.0 V-1.6 V vs. Na^+/Na) insertion into α-V_2O_5 at 0.1 C is shown in **Figure 3.9a**. The curve is smooth with none of the obvious plateaus indicating no phase-transition or redox reaction, and a capacity of ~80 mAh/g, significantly lower than the theoretical capacity of 147 mAh/g. CVs in **Figure 3.9b**, were conducted between 1.7V and 3.8V (vs. Na^+/Na) at rates between 0.1 mV/s - 0.6 mV/s. All show flat curves without peaks associated with redox reaction and only show background current increases with the scan rate. Galvanostatic rate performance is shown in **Figure 3.9c** with varying charge-discharge rates between 0.2 C to 2 C. Again, all curves are featureless and lack characteristic plateaus indicating ion insertion, consistent with the CV results. The specific capacity of the α-V_2O_5 cathode decreases quickly from 66 mAh/g at 0.2 C to 10 mAh/g at the fastest rate of 2 C. Finally, **Figure 3.9d** shows the capacity retention performance of α-V_2O_5 at a discharge rate of 1 C. The initial capacity is only ~15 mAh/g and decreases to ~13 mAh/g after 150 cycles, displaying a relatively stable but incredibly low capacity. The fluctuation of capacity appeared during cycling which might be caused by the instability of sodium-ion insertion-deinsertion in α-V_2O_5.

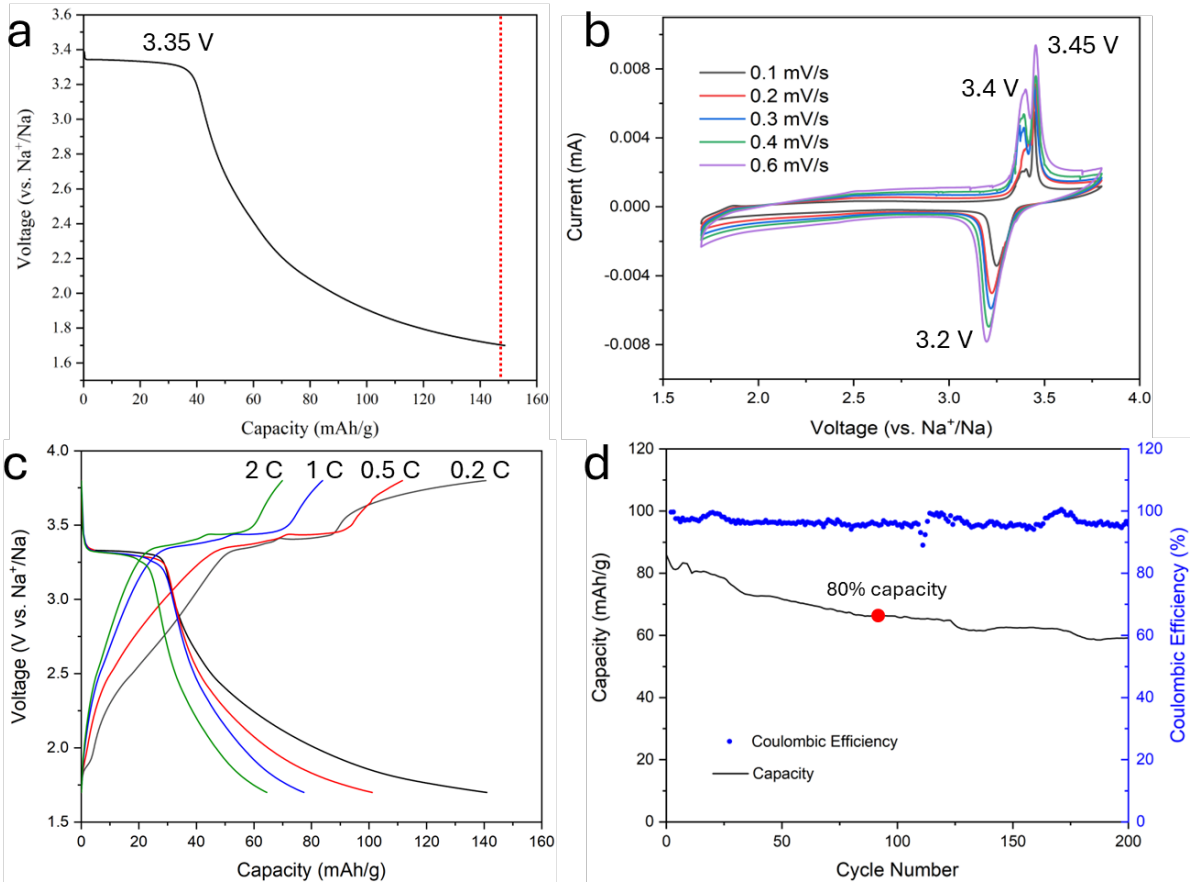

Figure 3.8. Electrochemical charge-discharge of γ'-V_2O_5/Na half-cell device. a) Galvanostatic Na ion insertion at C/10 rate with one Na ion insertion. b) CV of γ'-V_2O_5 cathode at different scan rates (done). c) Rate performance of γ'-V_2O_5 at different C-rates. d) Capacity retention of γ'-V_2O_5.

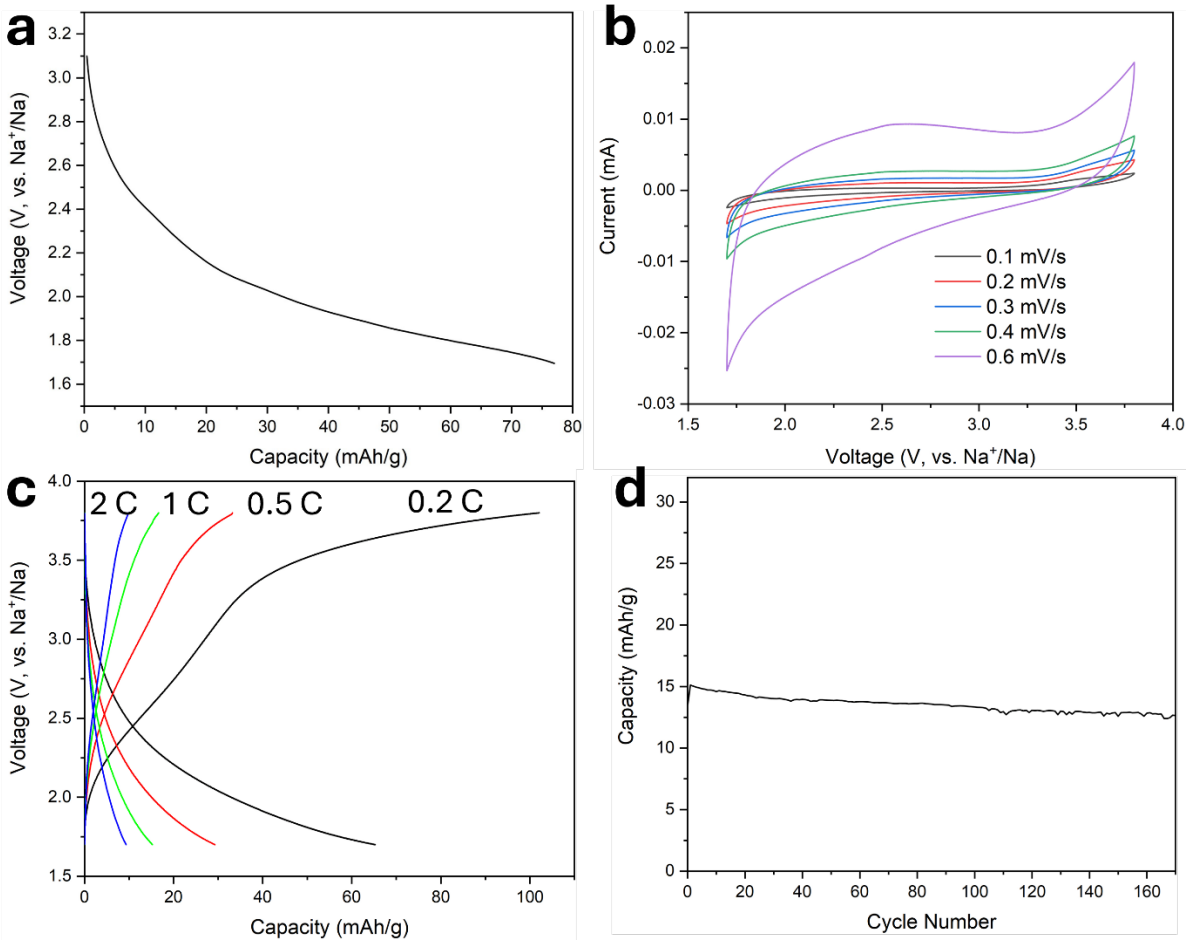

Figure 3.9. Electrochemical charge-discharge of α-V_2O_5/Na half-cell device. a) Galvanostatic Na ion insertion at C/10 rate with one Na ion insertion. b) Cyclic voltammograms (CVs) of α-V_2O_5 cathode at 0.1, 0.2, 0.3, 0.4, 0.6 mV/s respectively. c) Rate performance of α-V_2O_5 which charges and discharges at 0.2, 0.5, 1 and 2 C-rates respectively. d) Capacity retention performance of α-V_2O_5 which cycled at 1 C.

In comparison with the poor sodiation of α-V_2O_5 (Figure 3.9), γ'-V_2O_5 has a much better ability for sodium storage. The result of one-sodium insertion reaction in two-electrode beaker cell shows an ideal specific capacity (152 mAh/g) when discharging at 0.1 C-rate. The γ'-V_2O_5 thin film reported here has a high initial Coulomb efficiency of 98% (Figure 3.8d) which shows higher performance than that reported in the literature to date[52]. CVs show a small peak-shift of 40 mV when the scan rate increases from 0.1 mV/s to 0.6 mV/s. Charge-discharge curves at C-rates varying from 0.2-2 C display a decreasing specific capacity from 140 to 68 mAh/g which is similar

to previously reported γ'-V_2O_5 powder[49–51]. To summarize, γ'-V_2O_5 has an ideal performance for sodiation.

3.4 Challenges and Considerations for γ'-V_2O_5 Thin Film Electrodes

Electrochemical methods offer straightforward and precise control over lithiation depth, enabling tuning of crystal structure, electrical conductivity, and ionic conductivity in various material systems by adjusting the concentration of the inserted ions. In this study, we leveraged this precise control to structurally modify V_2O_5 films, successfully synthesizing advanced γ'-V_2O_5 electrodes specifically for SIB applications. Our electrochemical phase engineering approach capitalizes on the well-documented lithiation kinetics of the V_2O_5 system, eliminating the need for hazardous reagents such as NO_2BF_4 typically required to synthesize γ'-V_2O_5[49–51,83]. The synthesized electrodes exhibited theoretical capacities of 147 mAh/g, coupled with excellent coulombic efficiency (98%), demonstrating the practical efficacy of our approach.

While this investigation provides a specific instance of Li-ion-induced crystal structure engineering in V_2O_5, it also underscores a potentially versatile and broadly applicable methodology. This approach may not be inherently limited to lithium as the modifying ion, nor to V_2O_5 as the host material, nor energy storage as the application space. Alternative ions such as Na^+, K^+, Mg^{2+}, etc., could similarly induce phase modification, broadening the scope of applications beyond lithium-based systems. Furthermore, the technique could be applicable across diverse material morphologies and fabrication methods, including sputtering, evaporation, chemical vapor deposition (CVD), electrochemical deposition (ECD), as well as bulk powders and various nanostructured materials. Currently we are expanding and exploring this ion-induced crystal structure engineering methods to various material systems.

Active phase manipulation via electrochemical ion insertion recently emerged as a powerful approach in solid-state iontronic devices[92,93]. For instance, controlled insertion of Li-ions has been demonstrated to dynamically modulate the electrical conductivity of transistor channels, illustrating that ion-driven structural and electronic transformations can directly influence device functionality[94]. Our findings reinforce this perspective, suggesting broad applicability for ion-induced phase engineering. Specifically, this method may enable new classes of tunable materials for applications such as memristors, neuromorphic computing, sensors, and even photovoltaic technologies like perovskite solar cells, where precise control of crystal structure and electronic properties is critical. More broadly, we believe, this work highlights an emerging paradigm shift in materials engineering—moving beyond traditional chemical and physical synthesis methods toward deliberate, electrochemically driven ion manipulation as a versatile tool for advanced material design and synthesis.

In this work, we have demonstrated a novel synthesis route to produce high-quality γ'-V_2O_5 thin films, specifically tailored for sodium-ion battery (SIB) applications. Our synthesis method eliminates the need for hazardous reagents, such as NO_2BF_4, typically required to obtain the γ'-phase. The synthesized γ'-V_2O_5 exhibits superior electrochemical performance, delivering a near-theoretical specific capacity of 147 mAh/g with an exceptional coulombic efficiency of 98%, significantly surpassing previously reported values (~50% CE). The material maintains robust performance even at higher charge-discharge rates (70 mAh/g at 2 C), demonstrating suitability for practical SIB electrode applications and competitive performance compared to powder-based γ'-V_2O_5 synthesized with traditional methods.

More broadly, this electrochemical phase engineering technique represents a significant advancement in materials synthesis, particularly relevant in the emerging field of ionics and

iontronics, where ions, rather than electrons, serve as primary signal carriers. Our integrated approach—combining atomic layer deposition (ALD), electrochemical lithiation-driven phase modification, and controlled thermal annealing—presents a versatile platform to precisely manipulate and preserve desired material phases as indicated by both the superior sodiation (Figure 3.8a-d) and lithiation (Figure 3.9a-d) of γ'-V_2O_5. Comprehensive multimodal characterization using Raman spectroscopy, XRD, SEM, and electrochemical analyses confirmed both the structural integrity and electrochemical performance of the γ'-V_2O_5 films. Furthermore, the adaptability of this method to diverse material morphologies and substrates paves the way for novel device architectures and broader applications beyond energy storage, including tunable iontronic devices, sensors, and advanced electronic systems.

Chapter 4: A Three-Dimensional Nanopore Architecture Enabling Stable, High-Power Sodium-Ion Microbatteries

4.1 Chapter Summary

A three-dimensional nanoscale architecture originating from the techniques used for semiconductor manufacturing offers a powerful route to overcome ion-transport limitations in microscale electrochemical systems. Here we report a sodium-ion microbattery array based on a coaxial V_2O_5/Pt nanotube architecture embedded within anodic aluminum oxide (AAO) nanopores, forming vertically aligned nanotubular electrodes conformally integrated with Pt nanotube current collectors. This nanoconfined geometry shortens Na^+ diffusion pathways, enhances charge-transfer kinetics, and maintains electronic conduction across the microbattery array. The resulting device delivers a high areal capacity of 44 μAh cm^{-2} (corresponding to one Na^+ per V_2O_5), excellent rate capability up to 2 C, and exceptional cycling stability with 80% capacity retention after 720 cycles. Cyclic voltammetry and Trasatti/Dunn analysis reveal that 66% of the stored charge arises from surface-dominated processes enabled by the nanotube architecture, compared to only 19% in planar films. These results demonstrate that semiconductor-derived 3D architectures can be directly translated to sodium-ion systems, enabling high-power, long-life microbatteries and establishing a generalizable platform for nano-ionic device engineering.

4.2 Fabrication of Three-Dimensional Nanopore Microbatteries

As outlined in the Introduction, our group has been exploring the fundamental limits of ion transport in high–aspect ratio nanostructures, nanoconfined systems, and controlled interfaces for well over a decade[18,19]. Using standard semiconductor manufacturing processes, we have demonstrated in both liquid and solid-state lithium-ion systems that nanostructuring electrodes enables a decoupling of power and energy density, while simultaneously providing a well-defined testbed for probing ion-transport limits in dense, three-dimensional electrode arrays. Through multiple platforms, this work has shown that nanoscale architectural control facilitates rapid ion and electron transport, leading to substantial improvements in rate capability and cyclability in lithium-based systems. These results raise a central question: whether architectural strategies that successfully mitigate transport limitations in Li-ion devices can be extended to sodium-ion systems, where ion mobility is intrinsically slower and materials compatibility is far more restrictive.

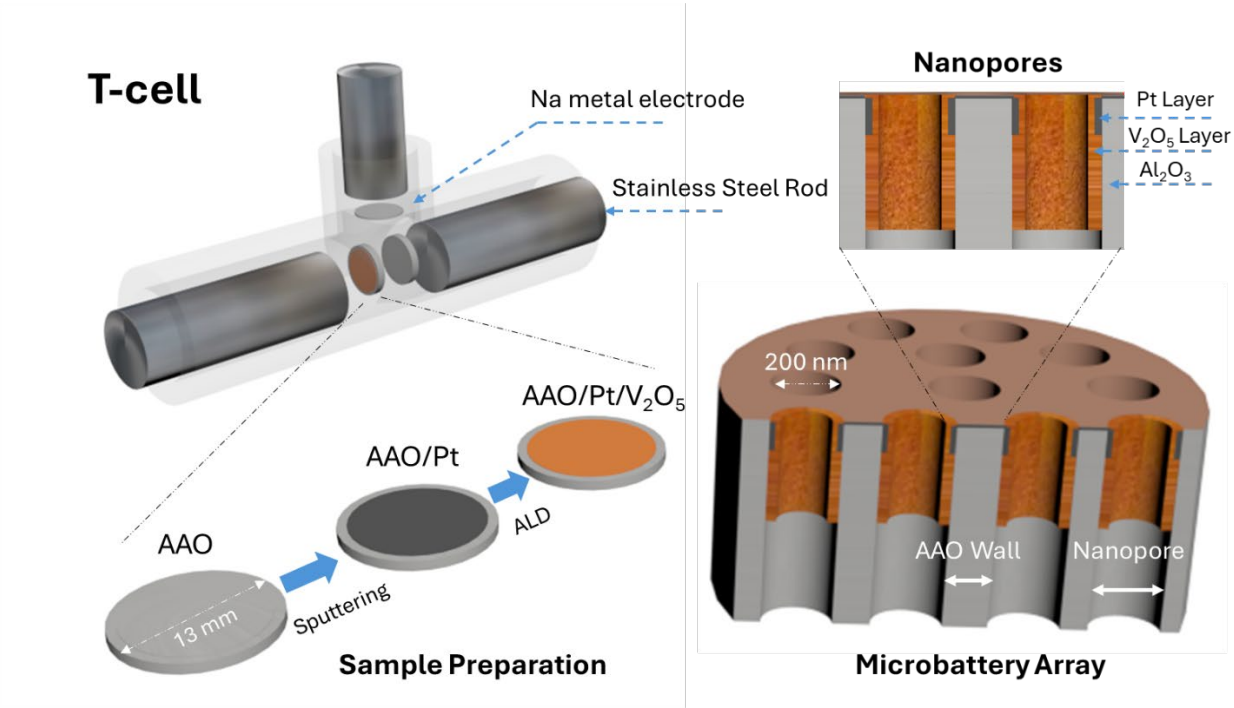

Figure 4.1 Nanopore battery configuration. The schematic shows the constitution of T-cell device as an electrochemical test platform for the following measurements. The integrated microbattery array is shown next to T-cell, having a uniform porous microstructure with deposited Pt and V_2O_5 layers. We have to notice that Pt layers (black part) are wrapped within V_2O_5 layers (dark yellow part), so they can only be observed from cross-section view.

To address this question, we modified our nanopore microbattery platform to enable systematic testing in sodium-ion systems. We designed and fabricated a symmetric nanopore sodium-ion microbattery within an anodic aluminum oxide (AAO) template, as diagramed in Figure 4.1, to investigate the effect of electrode nanostructuring on sodium-ion electrochemistry. The uniformly distributed nanopores of the AAO template provide an ideal substrate for atomic layer deposition (ALD), enabling the fabrication of highly conformal and uniform microbattery arrays. In this architecture, all components of the microbattery are embedded within a single nanopore, while the array of pores within the AAO template forms a microbattery array.

The AAO template defines the geometry of the nanopore microbatteries, with a pore diameter of 200 nm and a pore length of 50 μm (Figure 4.2a). The AAO disks have a diameter of 0.6 cm, with the disk thickness equal nanopore length (50 μm). The center-to-center pore spacing is approximately 450 nm. Platinum was selected as the current collector due to its high conductivity and electrochemical inertness. A Pt layer with an equivalent planar thickness of 25 nm was deposited by sputtering. The thickness and conformality of the Pt deposition were confirmed by cross-sectional SEM (Figures 4.2b and 4.2c) and EDS (Figure 4.2d). The SEM images show a distinct Pt layer of approximately 25 nm at the top of the nanopores, while cross-sectional EDS analysis indicates a Pt signal extending to a depth of approximately 5 μm within the AAO template.

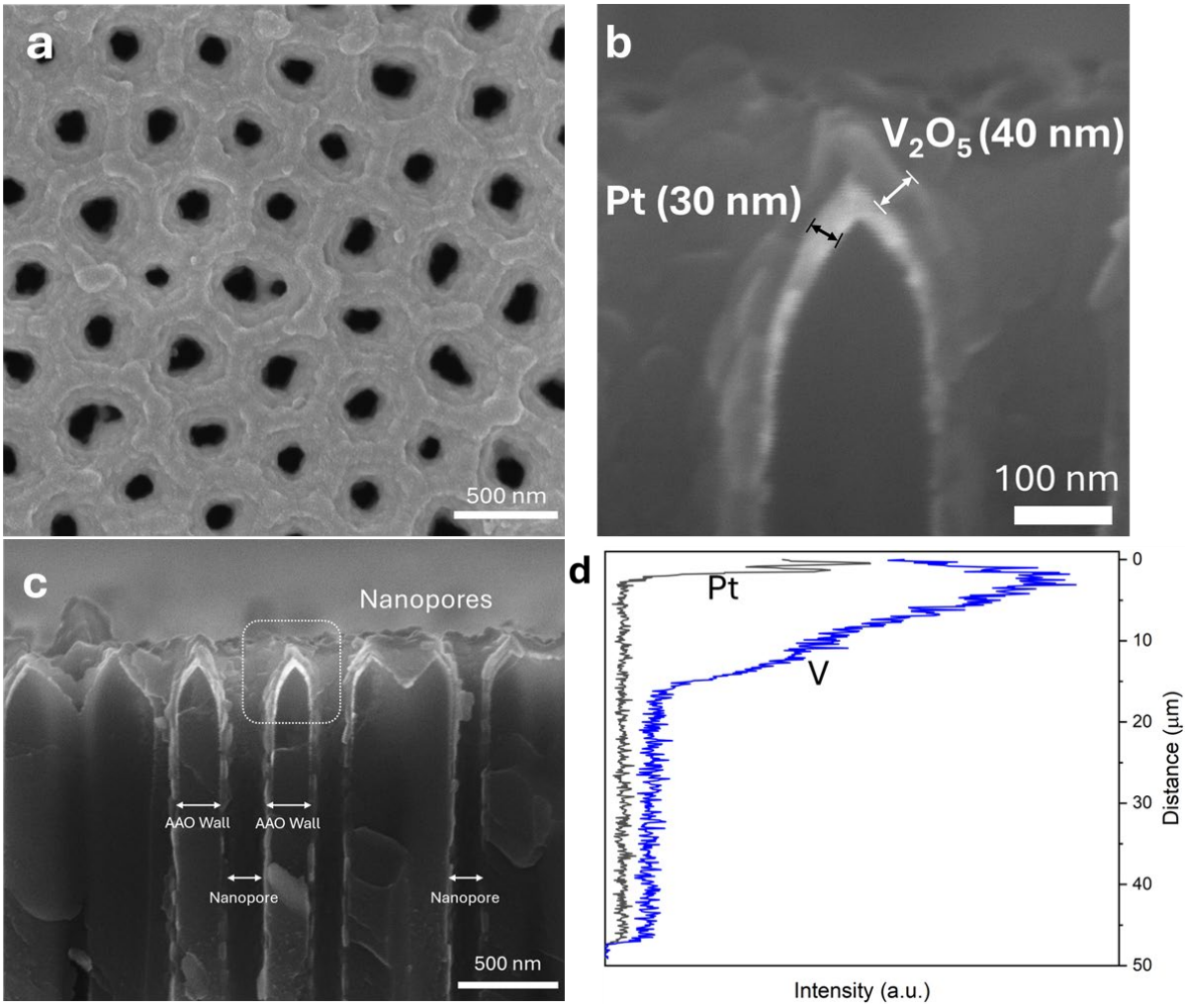

Figure 4.2 Metrology of 3D nanopore battery. a, SEM image of the device (top view), showing the AAO nanopore pattern after the preparation of γ'-V_2O_5 electrodes. **b,** SEM image of the device (cross-section view), showing the layered structure of the deposited V_2O_5 and Pt material. **c,** SEM image of the device (cross-section view), showing the full-field-of-view of AAO morphology. **d,** EDS line scan of device cross-section, demonstrating the content of Pt and V respectively.

γ′-V_2O_5 was chosen as the active electrode material based on previous results[68]. Each T-cell has ~310 μg V_2O_5 as the working and counter electrode. Both V_2O_5 electrodes have already been presodiated to $Na_{0.5}V_2O_5$. The V_2O_5 was deposited onto the Pt-coated AAO template using a previously published ALD process, producing amorphous V_2O_5 that was subsequently converted to crystalline γ′-V_2O_5 through a post-deposition treatment described in the Materials and Methods section[53,68]. The thickness of the γ′-V_2O_5 layer was confirmed by cross-sectional SEM and EDS

(Figures 4.2b–d). The γ′-V_2O_5 thickness at the top of the nanopores is approximately 25 nm, and the V signal extends to a depth of approximately 20 μm, indicating uniform and conformal deposition along the nanopore walls.

As diagramed in Figure 4.1, each completed three-electrode T-cell consists of two γ′-V_2O_5 3D nanopore electrodes serving as the working and counter electrodes, along with a metallic sodium reference electrode. The electrolyte was 1 M $NaClO_4$ in propylene carbonate/ethylene carbonate (PC/EC, 1:1 by volume). Prior to cycling, the working and counter electrodes were externally shorted and held at 3.1 V (vs. Na/Na^+) for 5 h to simultaneously pre-sodiate both electrodes to $Na_{0.5}V_2O_5$. The connection of the circuit for presodiation and more details are shown in Figure 4.3. This presodiation voltage was optimized over the range of 3.0–3.3 V, and a holding voltage of 3.1 V was found to reliably produce $Na_{0.5}V_2O_5$ electrodes (Figure 4.4).

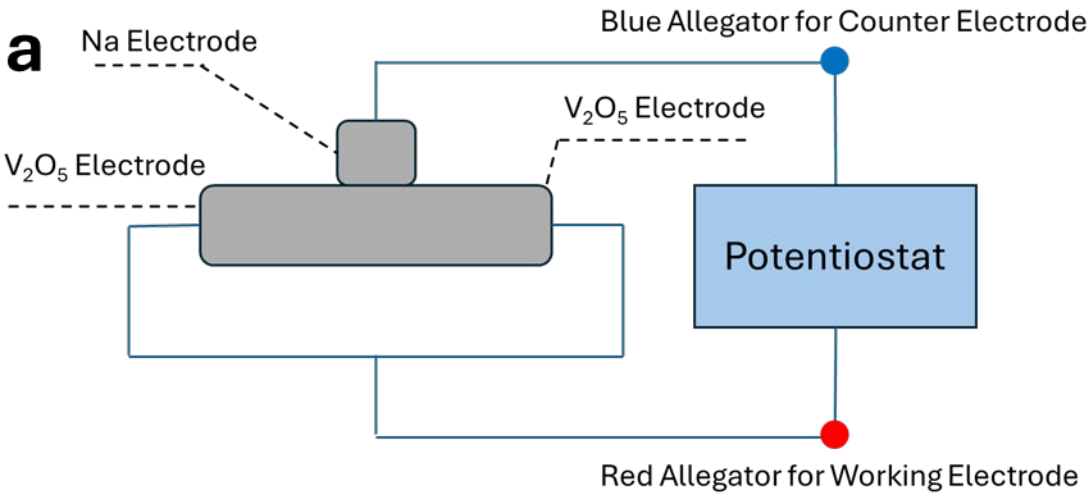

Fig. 4.3. (a) Schematic diagram of the circuit connection for presodiation of both V_2O_5 electrodes. The two V_2O_5 electrodes of the T-cell are short and connected to the potentiostat to be sodiated to the same extent. **(b)** Picture of T-cell and the corresponding circuit for presodiation.

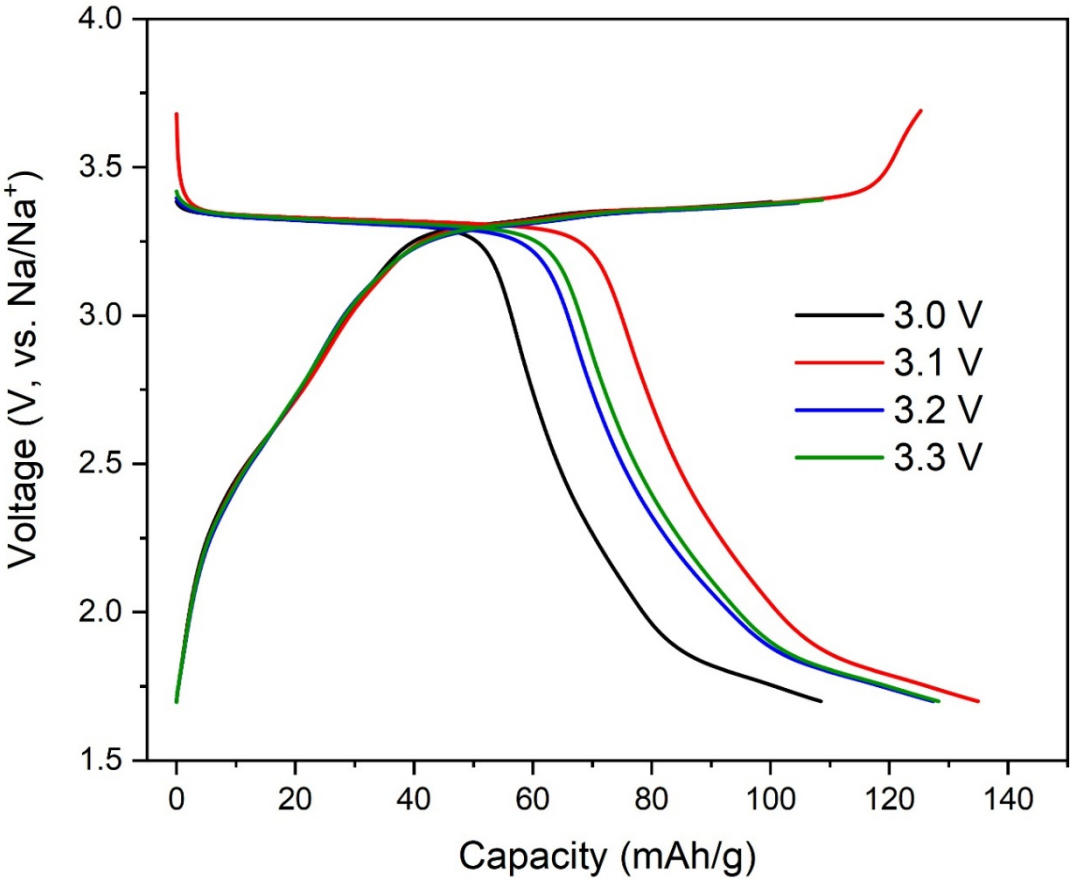

Fig. 4.4. Electrochemical charge-discharge of T-cell after predsodiation process. Both V_2O_5 electrodes of T-cell were presodiated and held at a specific voltage for 5 h during the presodiation process to get rid of electrochemical polarization effect. In order to get a complete sodiation-desodiation of V_2O_5 electrodes, 3.0-3.3 V were tested to find the appropriate holding voltage value. Only 3.1 V provides a complete voltage range (1.7-3.8 V) during cycling.

In order to properly elucidate the advantages of 3D nanosarchitectures we made a mass balanced planar control sample. We normalized the per unit area mass loading of the 3D γ′-V_2O_5 nanopore electrodes to be 323 μg/cm^2. This calculates to an equivalent planar thickness of ~ 1 um (See the calculation under Figure 4.5 for additional details). Planar samples were fabricated on 1 cm^2 Si wafers coated with 50 nm of Pt via sputtering and 1 μm of ALD V_2O_5 using the same recipe for the 3D samples. The control group electrochemistry was conducted in a two-electrode beaker cell (γ′-V_2O_5 vs. Na/Na$^+$). A diagram of the configuration of the beaker cell is shown in Figure 4.5.

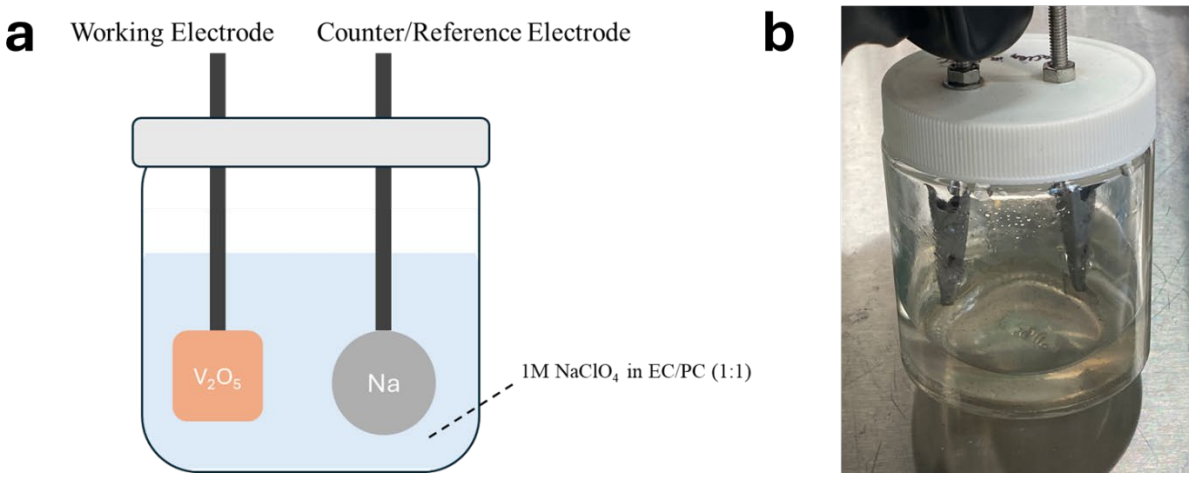

Fig. 4.5. (a) Configuration of the beaker cell for electrochemical measurements of control gruop. **(b)** Self-made beaker cell. The allegators were fixed to be the holder for electrode materials, as shown by red circle.

Calculation to Normalize the Specific Capacity of Working and Control Groups

To compare the rate performance of γ′-V_2O_5 3D nanopore electrodes and γ′-V_2O_5 2D thin-film electrodes, we normalized the per unit area mass loading to make sure the specific capacity would not affect the comparison. Both groups have the specific capacity of 47.6 μAh/cm^2, and the calculation is as follows.

The footprint pattern of 3D microbattery array is circular which has a radius of 0.55 cm, and the mass of γ′-V_2O_5 material is 315 μg. Therefore, the per unit area mass loading of γ′-V_2O_5 is

$$m = 315\ \mu g/(\pi \times (0.55\ cm)^2) = 323\ \mu g/cm^2$$

The specific capacity is $Q = \frac{m}{M_{V2O5}} \times F = \frac{323\ \mu g/cm^2}{181.88\ g/mol} \times 96485 \frac{C}{mol} = 47.6\ \mu Ah/cm^2$.

Since the control group is the square wafer with sides of 1 cm, we can calculate the thickness of planar V_2O_5 layer: $l = \frac{m}{d_{V2O5}} = 323\ \mu \frac{g}{cm^2}/(3.35\ g/cm^3) = 0.96\ \mu m$

4.3 Performance and Challenges for the Electrochemical Test Platform

4.3.1 Electrochemical sodiation-desodiation of symmetric full cell

The electrochemical performance of the 3D nanopore sodium-ion microbattery is shown in Figures 4.6 and 4.7. Figure 4.6a shows a representative galvanostatic (1/10 C) discharge curve. These data show a specific capacity of 44 μAh cm^{-2} with a plateau at approximately 3.3 V vs. Na/Na^+ corresponding to a one–sodium-ion insertion reaction in the 3D γ′-V_2O_5 nanopore electrodes.

Cyclic voltammograms (CVs) were recorded over a potential range of 1.7–3.8 V vs. Na/Na^+ (Figure 4.6b), consistent with the insertion of one sodium ion per unit cell of γ′-V_2O_5. The spectra exhibit two well-resolved oxidation peaks at approximately 3.3 and 3.4 V and a corresponding set of reduction peaks near 3.2 V. The redox peak distribution is consistent with our prior work on thin-film V_2O_5 electrodes and confirms a one-sodium-ion insertion reaction occurring within the nanotubular γ′-V_2O_5 electrodes. The sharpness of the peaks indicates a highly reversible sodium insertion process. As the scan rate increases from 0.1 to 0.5 mV s^{-1}, the redox peak separation increases to approximately 48 mV, reflecting near lithium-like kinetics compared to lithium-ion insertion in V_2O_5, where peak shifts are typically ~30 mV over the same scan-rate range[19].

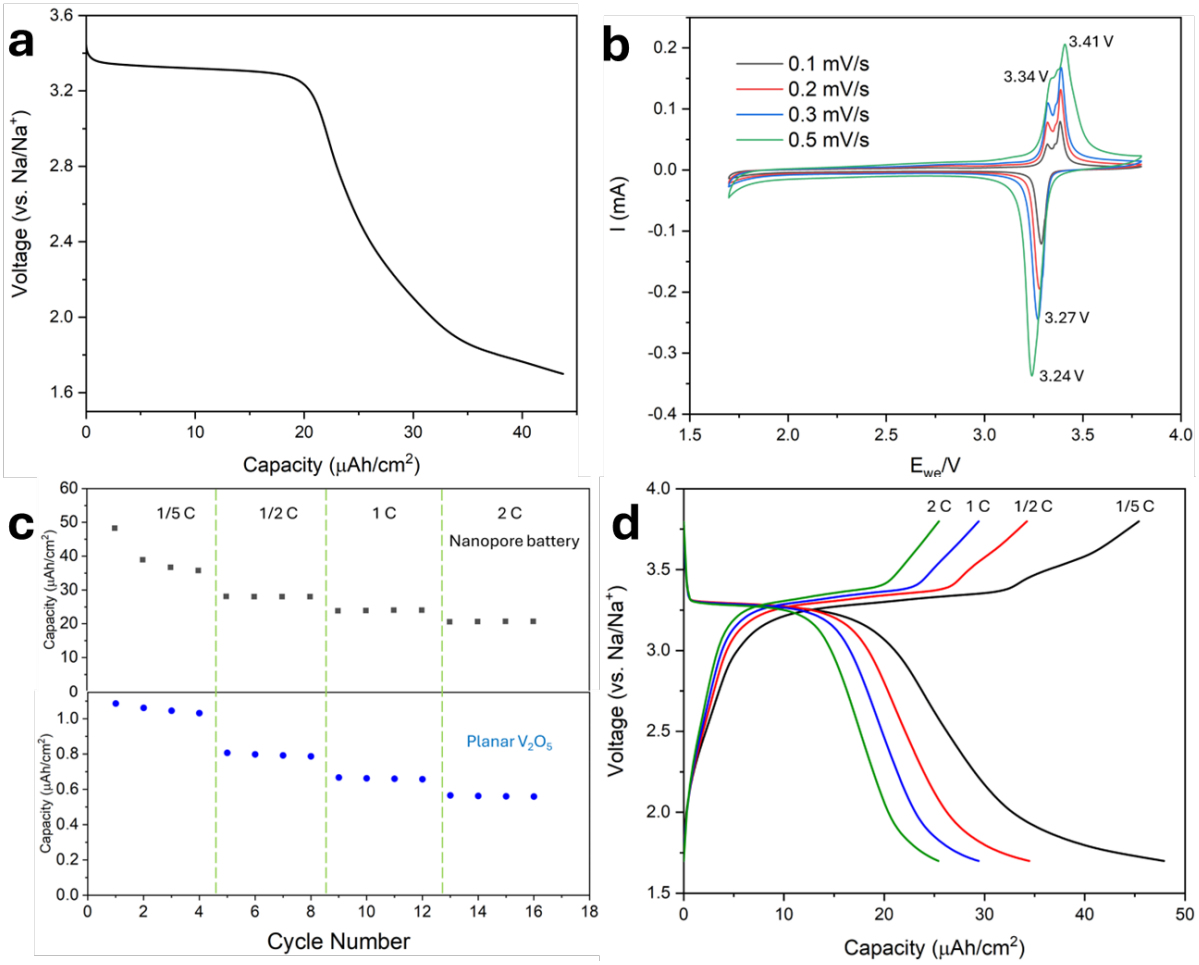

Figure 4.6 Electrochemical sodiation-desodiation of symmetric full cell. a, Galvanostatic Na ion insertion at 1/10 C. **b,** CVs of V_2O_5/Pt nanotube electrode at different scan rates. **c,** Rate performance of nanopore battery (black) and control device with planar V_2O_5 electrode (blue). **d,** Galvanostatic charge-discharge cycling curves of V_2O_5/Pt nanotube electrode at various C rates.

The rate performance of the 3D nanopore sodium-ion microbattery, compared with a mass-balanced planar V_2O_5 control electrode, is shown in Figure 4.6c. The symmetric full cell exhibits excellent rate capability, maintaining high specific capacity across increasing charge–discharge rates. Specific capacities of 48 μAh cm^{-2} at 1/5 C, 34.6 μAh cm^{-2} at 1/2 C, 29.5 μAh cm^{-2} at 1 C, and 25.4 μAh cm^{-2} at 2 C are observed. In contrast, the planar V_2O_5 control electrode delivers a specific capacity of approximately 1 μAh cm^{-2} at 1/5 C, which decreases to ~0.6 μAh cm^{-2} at 2 C. This pronounced difference confirms that nanostructuring provides a similar kinetic enhancement

of electrochemical performance in sodium-ion systems as previously observed in lithium-ion systems.

Galvanostatic charge–discharge curves of the 3D γ′-V_2O_5 electrodes as a function of C-rate are shown in Figure 4.6d. The discharge plateau remains centered near 3.2 V across all rates, indicating stable reaction thermodynamics despite increasing current density. The delivered capacity decreases from approximately 50 µAh cm^{-2} at 1/5 C to ~25 µAh cm^{-2} at 2 C, consistent with the rate-performance trends observed in Figures 4.6a and 4.6c.

4.3.2 The long-term cycling performance of the 3D nanopore sodium-ion microbattery

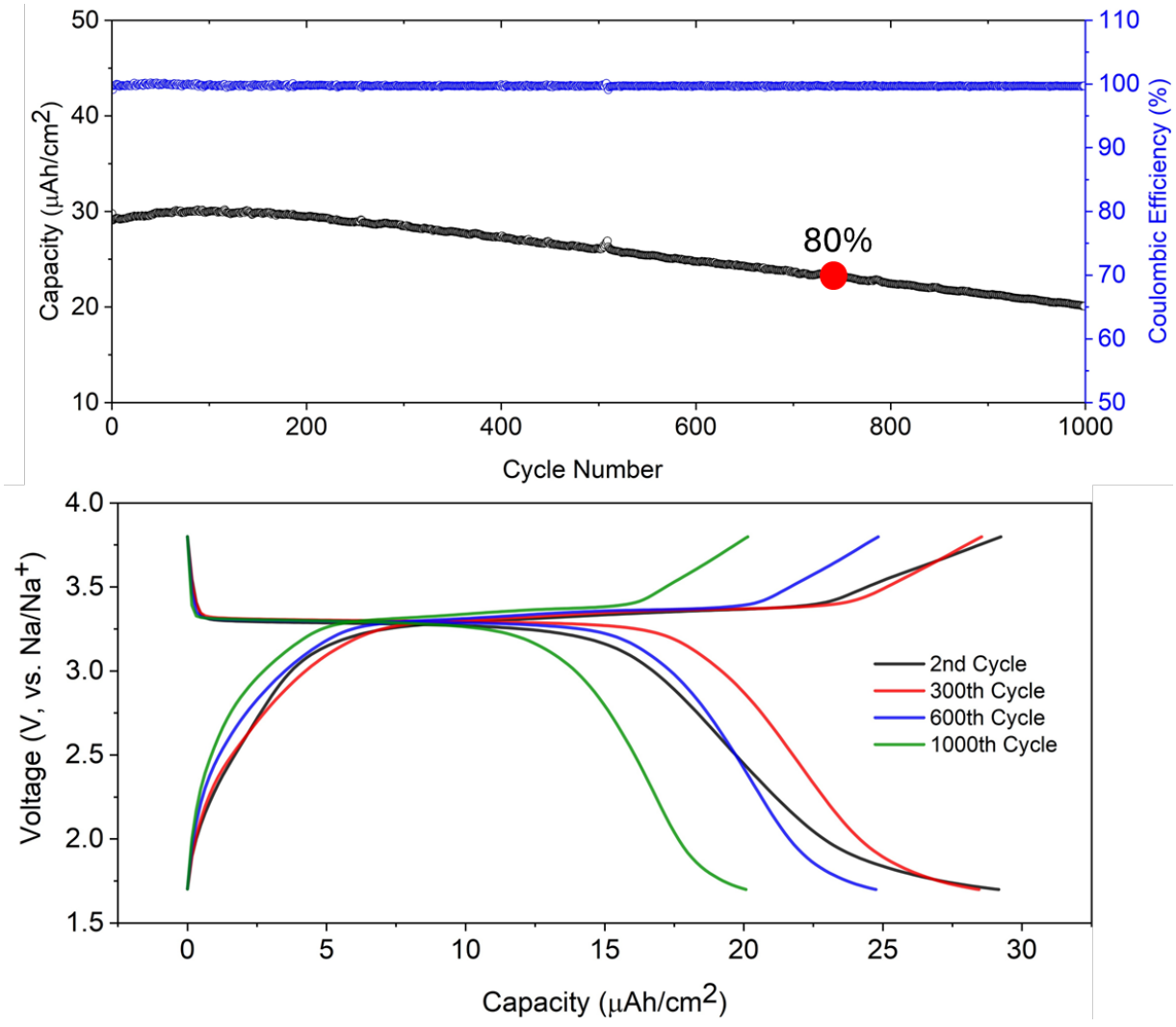

Figure 4.7 Capacity retention of symmetric full cell. a, V_2O_5/Pt nanotube electrode has 80% of the original capacity after cycling for 720 cycles at 1 C. **b,** Charge-discharge curves at the 2nd, 300th and 600th cycles.

The long-term cycling performance of the 3D nanopore sodium-ion microbattery is shown in Figure 4.7a and 4.7b. The 3D γ′-V_2O_5 nanotube architecture exhibits an excellent charge–discharge lifetime, retaining approximately 80% of its initial specific capacity after 720 cycles at 1 C (Figure 4.7a). The cell exhibits a Coulombic efficiency exceeding 99.5% throughout extended cycling, indicating minimal parasitic reactions and highly reversible Na^+ insertion/extraction. This high reversibility directly contributes to the outstanding capacity retention. This cycle life substantially exceeds that typically reported for commercial and laboratory-scale sodium-ion battery systems, which often exhibit capacity fade within a few hundred cycles under comparable conditions[64–68,74,95]. And higher than reported for similar nanostructured systems discussed in the introduction.

Representative galvanostatic charge–discharge curves from the 2nd, 300th, 600th and 1000th cycles (Figure 4.7b) show nearly identical plateau positions associated with one-sodium-ion insertion and deinsertion, indicating stable phase transitions throughout extended cycling. The preservation of plateau voltage further reflects a stable electrochemical reaction and consistent reversibility throughout the lifetime of the device. Together, these results demonstrate the exceptional cyclability and capacity retention enabled by the nanopore battery architecture, confirming that nanoscale architectural control plays a dominant role in stabilizing sodium-ion electrochemistry compared to planar V_2O_5 electrodes.

4.3.3 Deconvolution of Charge Contributions

Trasatti's method[96] and Dunn's method[97] were used to deconvolute and compare the charge-storage mechanisms observed in the 3D nanopore electrodes and planar control samples.

The results are summarized in Figures 4.8a–c and Figures 4.9. In general, total charge storage in electrodes consists of contributions from surface-dominant processes including the electrical double-layer and fast Faradaic surface reactions, and diffusion-dominated Faradaic processes associated with ion insertion. The surface-dominant reaction current scales linearly with scan rate (v), whereas the diffusion-dominated contribution scales with the square root of scan rate ($v^{1/2}$). The analysis of Trasatti's method is based on the following equations:

$$If\ v \to \infty,\ C \to C_s, so\ C = \frac{const.}{\sqrt{v}} + C_s$$

$$If\ v \to 0, C \to C_s + C_i, so\ \frac{1}{C} = const. \cdot v^{1/2} + \frac{1}{C_s + C_i}$$

Trasatti's method determines the total capacitance ($C_T = C_s + C_i$) by extrapolating to infinitely slow scan rates—representing the limit in which even the most kinetically hindered insertion processes have sufficient time to complete—while the surface capacitance C_s is obtained by extrapolating to infinitely fast scan rates, isolating only the processes fast enough to respond instantaneously. Although these limits are physically unrealizable, they provide a self-consistent framework for bounding the total charge and its surface-dominant fraction. The difference between these values ($C_i = C_T - C_s$) corresponds to the capacitance associated with diffusion-limited ion-insertion processes. Dunn's method complements this picture by decomposing the charge contributions at each potential, providing a voltage-resolved map of surface-dominant and diffusion-limited processes contributions across the electrochemical window.

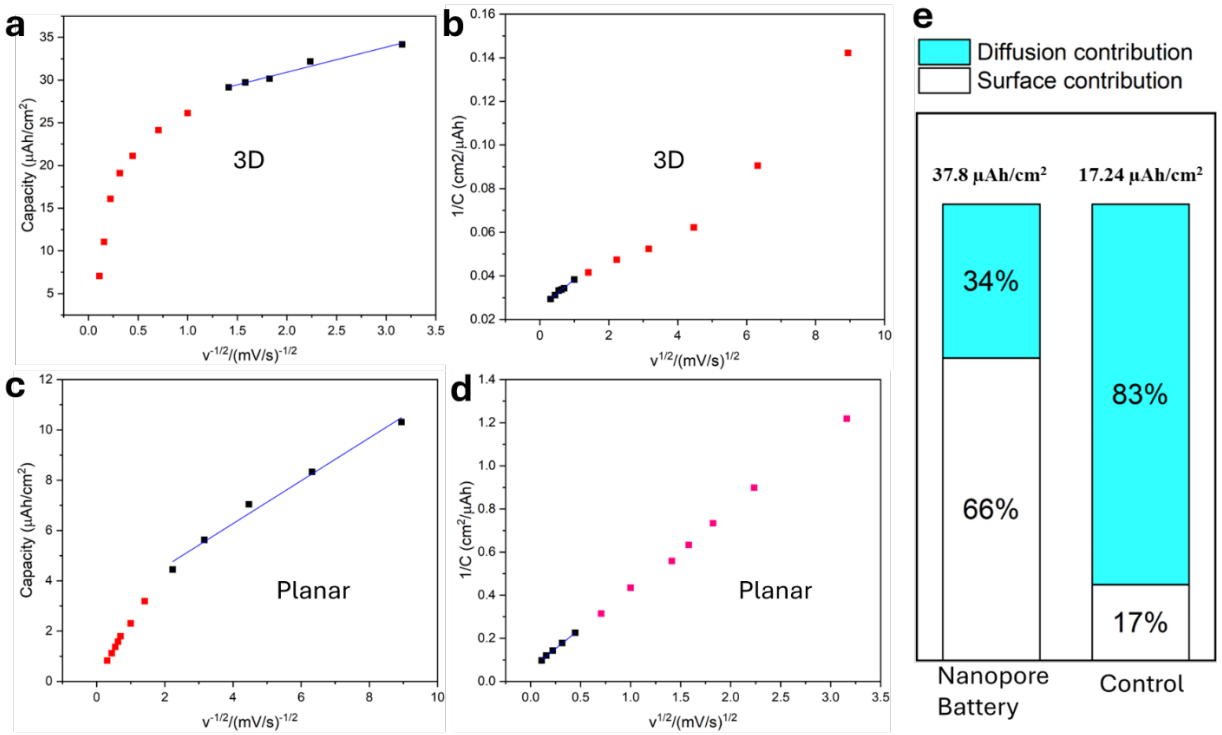

Figure 4.8 Deconvolution of charge contributions from CVs (Trasatti's method). The result of Trasatti's method for V_2O_5 nanotube electrodes shows **a,** Gravimetric capacity vs. inverse square root of scan rate for V_2O_5/Pt nanotube electrodes. The Intercept value represents the charge proportional to scan rate (v), which is 25.0 μAh/cm^2. **b,** Inverse gravimetric capacity vs. square root of scan rate for V_2O_5/Pt nanotube electrodes. The inverse of the intercept is the total charge (37.8 μAh/cm^2). The results of Trasatti's method for planar V_2O_5 electrodes include **c,** Specific capacity vs. inverse square root of scan rate for planar V_2O_5 electrodes. The intercept value represents the surface-dominant capacity, which is 2.8 μAh/cm^2. **d,** Reciprocal capacity vs. square root of scan rate for planar V_2O_5 electrodes. The inverse of the intercept value is the total charge (17.24 μAh/cm2). **e,** V_2O_5/Pt nanotube electrodes have 66% capacity contributed by surface reaction in comparison with 17% surface contribution of planar V_2O_5 electrodes.

For the 3D nanopore electrodes, the surface-dominant capacitance was first extracted by plotting capacitance (C) as a function of the inverse square root of scan rate ($v^{-1/2}$) over the range of 0.1–3.5 mV/s, as shown in Figure 4.8a. Using the linear region between 0.1 and 0.5 mV/s, the intercept representing surface-dominant capacity (Cs) was determined to be 25.0 μAh/cm². The total capacitance (C_T) was then obtained by plotting the reciprocal capacitance (1/C) as a function of the square root of scan rate ($v^{1/2}$), shown in Figure 4.8b. From the same linear region, a total

capacitance of 37.7 μAh/ cm² was extracted, yielding an insertion-dominant capacitance (C_i) of 12.7 μAh/cm². Analogous analysis was performed for the planar γ′-V_2O_5 control electrodes. The intercept of the capacitance versus $\nu^{-1/2}$ plot corresponds to a surface-dominant capacity of 2.8 μAh/cm² (C_s). From the reciprocal capacitance versus $\nu^{1/2}$ plot, the inverse of the intercept yields a total capacitance of 17.24 μAh/cm² (C_T), resulting in an insertion-dominant capacitance of 14.44 μAh/cm² (C_i).

A direct comparison between the planar and 3D electrodes is summarized in the bar charts shown in Figure 4.8e. The 3D nanopore electrodes are dominated by surface-controlled charge storage, with approximately 66% of the total capacity arising from surface-dominant processes and 34% from diffusion limited-ion insertion. In contrast, the planar γ′-V_2O_5 electrodes are dominated by diffusion-limited Faradaic insertion, with approximately 83% of the capacity arising from bulk ion insertion and only 17% from surface-dominant contributions (Figure 4.8c).

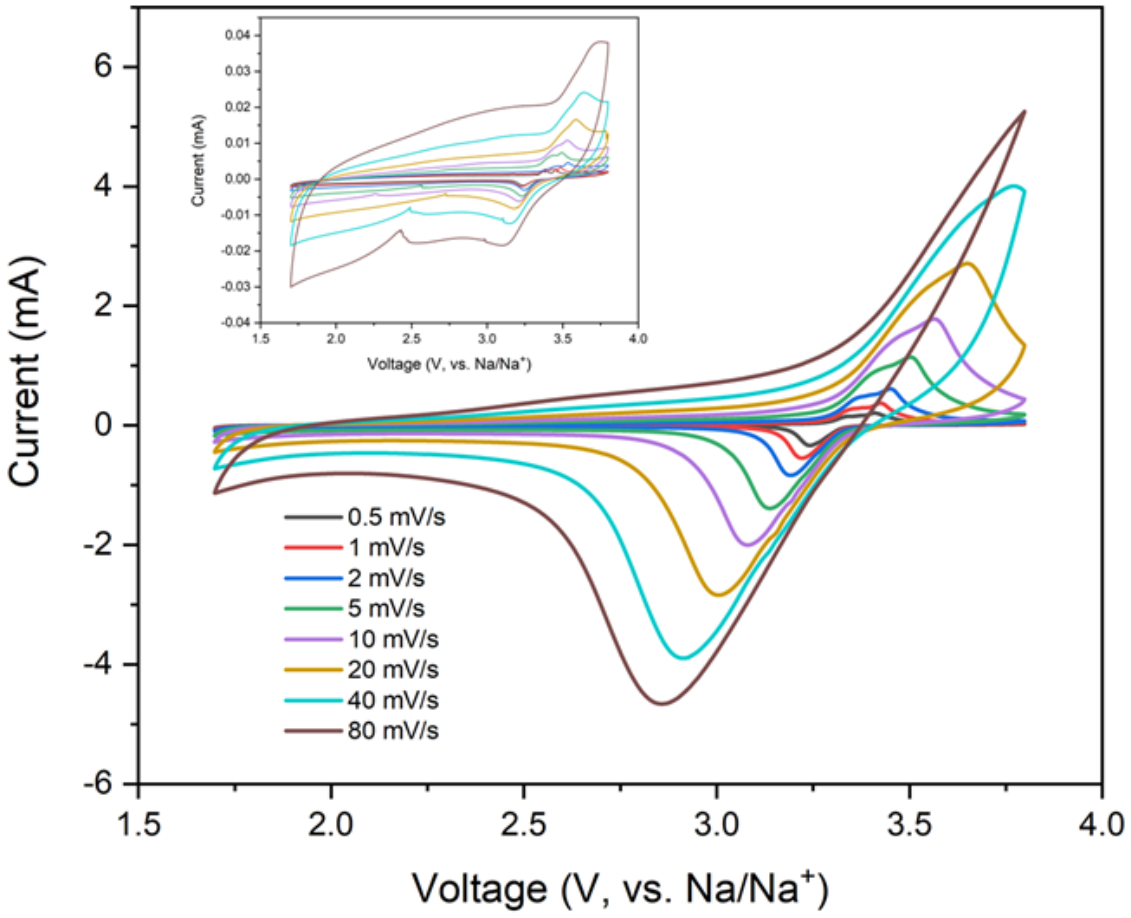

Fig. 4.9. Trasatti's method for V_2O_5 nanotube electrodes and planar V_2O_5 electrodes. CVs of V_2O_5 nanotube electrodes showing characteristic oxidation and reduction peaks with scan rates up to 80 mV/s. Inset: CVs of planar V_2O_5 electrodes with the same scan rates, also showing characteristic oxidation and reduction peaks but with lower peak intensity.

These results further confirm that the coaxial γ′-V_2O_5/Pt nanotubular architecture in sodium-ion systems produces a similar effect to that previously observed in lithium-ion systems, facilitating more efficient charge transfer at the electrode surface. Consistent with the rate-performance results discussed in the previous section, the high surface area and thin active layers of the nanotube structure enable electrochemical access to a larger fraction of the stored charge. Together, these findings demonstrate that nanoscale architectural control provides an effective strategy for balancing cell capacity and energy density while mitigating the kinetic limitations associated with sodium-ion insertion.

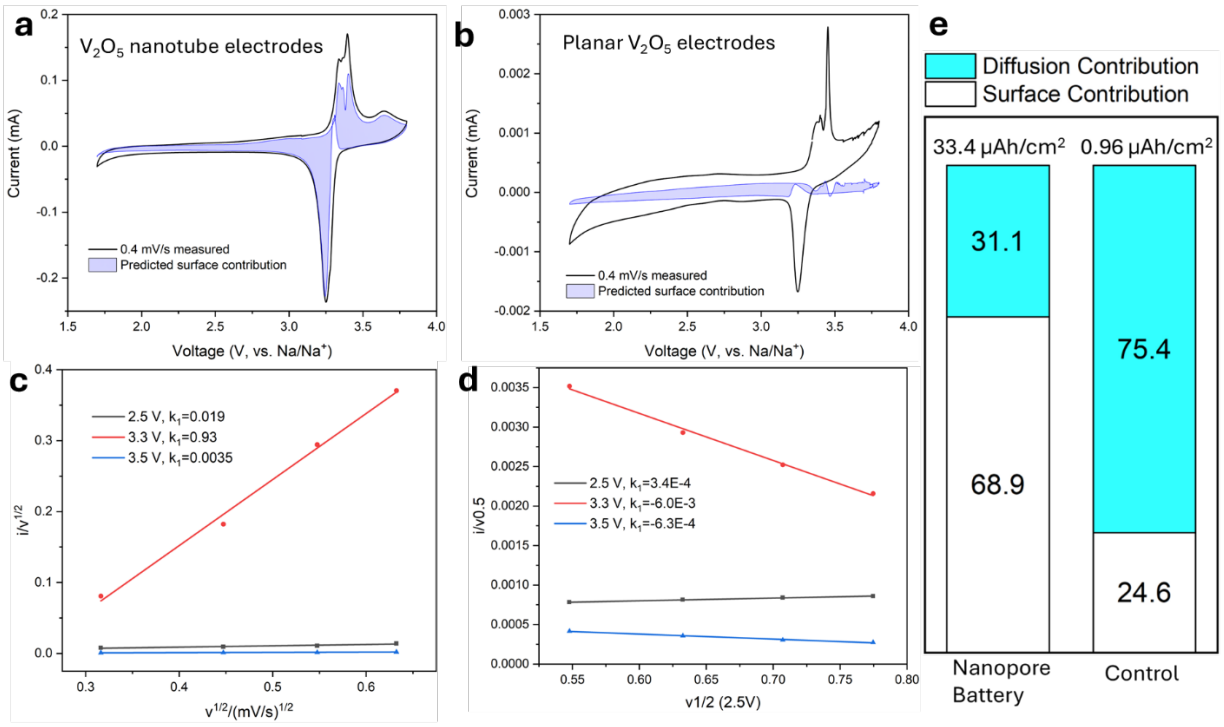

Figure 4.10 Deconvolution of charge contributions from CVs (Dunn's method). The results of Dunn's method show **a,** V_2O_5 nanotube electrodes' CV curve (black solid line) measured at 0.4 mV/s and blue shaded area which represents surface-dominant contribution (68.9%). **b,** planar V_2O_5 electrodes' CV curve (black solid line) measured at 0.4 mV/s and blue shaded area which represents surface-dominant contribution (24.6%). **c,** the fitting curves ($i/v^{1/2}$ vs. $v^{1/2}$) to get surface contribution coefficient k_1 of V_2O_5 nanotube electrodes at 2.5 V, 3.3 V, and 3.5 V respectively. **d,** the fitting curves ($i/v^{1/2}$ vs. $v^{1/2}$) to get surface contribution coefficient k_1 of planar V_2O_5 electrodes at 2.5 V, 3.3 V, and 3.5 V respectively. **e,** V_2O_5 nanotube electrodes have 68.9% capacity contributed by surface reaction in comparison with 24.6% surface contribution of planar V_2O_5 electrodes.

Dunn's method[97] complements the analysis provided by Trasatti's method by resolving surface-dominant and diffusion-limited contributions at each potential across the CV window. For a given voltage, the total measured current can be expressed as:

$$i(V) = k_1 v + k_2 v^{1/2}$$

where the $k_1 v$ term represents the surface-controlled contribution scaling linearly with scan rate, and the $k_2 v^{1/2}$ term represents the diffusion-limited contribution. By plotting $iv^{-1/2}$ versus $v^{1/2}$ at each recorded voltage across the five scan rates (0.1, 0.2, 0.3, 0.5, and 0.6 mV/s), the coefficient k_1 is extracted by linear fitting. The surface-controlled current at each voltage is then compared directly against the measured CV spectrum to yield a voltage-resolved map of the surface-

dominant charge fraction. Applying this analysis to the 3D nanopore and planar electrodes (Figure 4.10c and d), the surface-dominant contributions are 68.9% and 24.6%, respectively. The results are summarized in the bar charts of Figure 4.10e and show close agreement with the values obtained from Trasatti's method, see Figure 4.8e.

These results further confirm that the coaxial γ′-V_2O_5/Pt nanotubular architecture in sodium-ion systems produces a similar effect to that previously observed in lithium-ion systems, facilitating more efficient charge transfer at the thin nanotubular electrode layer. Consistent with the rate-performance results discussed in the previous section, the high surface area and thin active layers of the nanotube structure enable electrochemical access to a larger fraction of the stored charge. Together, these findings demonstrate that nanoscale architectural control provides an effective strategy for balancing cell capacity and energy density while mitigating the kinetic limitations associated with sodium-ion insertion.

4.4 Future Considerations for the Three-Dimensional Nanoscale Architecture of Batteries

In this work, we designed a nanopore battery array as a controlled electrochemical test platform to investigate sodiation within a nanoscale, nanoconfined environment. The device architecture consists of a V_2O_5/Pt coaxial nanotube electrode structure embedded within an anodic aluminum oxide (AAO) template, with liquid electrolyte filling the nanopores. This platform, combined with our previous work, directly leverages semiconductor manufacturing concepts, i.e. high-aspect-ratio structures, conformal deposition, and parallel device integration, to interrogate ion transport and electrochemical behavior under well-defined geometric constraints.

In lithium-ion systems, we and others have shown that thin active layers combined with uniform nanopore architectures significantly shorten ion diffusion pathways, while coaxial metallic current collectors facilitate efficient electron transport [17–19]. Together, these effects enable

high power density, long cycle life, and decoupling of energy and power through architectural design. Given the demonstrated impact of nanoscale architecture on electrochemical performance, it was a natural question whether the same design principles could be extended to sodium-ion batteries, despite the intrinsically slower kinetics of Na^+ transport and interface issues witnessed in solid-state sodium microbatteries[23]. Using atomic layer deposition, sputtering, and electrochemical phase engineering developed in our prior work, we integrated γ′-V_2O_5/Pt coaxial nanotube electrodes into AAO nanopores (Figure 4.2) and directly compared their performance to planar γ′-V_2O_5 electrodes (Figures 4.6 and 4.7).

The resulting sodium-ion nanopore microbatteries exhibit dramatically improved performance across all key metrics. Compared to planar electrodes, the nanopore architecture delivers specific capacities that are higher by approximately two orders of magnitude over the range of 0.2–2 C as seen in Figure 4.6c. More importantly, Figure 4.7a, the 3D nanopore sodium-ion microbattery retains 80% of its initial capacity after more than 700 charge–discharge cycles at 1 C, representing more than a tenfold improvement in cycle life relative to planar γ′-V_2O_5 electrodes, which typically fail after ~70 cycles under similar conditions. These results demonstrate that the nanoscale architectural control successfully mitigates the poor rate capability and short cycle lifetime normally associated with sluggish sodiation kinetics in V_2O_5. Notably, the cycling stability achieved here compares favorably with mature commercial sodium-ion battery chemistries based on Prussian blue analogues[98], which typically operate at lower voltages (~1.56 V) and deliver capacities of ~67 mAh g^{-1} at 1 C. Together, these observations confirm that nanostructured architectures provide a viable route to fully accessing the high theoretical capacity of V_2O_5 in sodium-ion systems.

Beyond the specific materials system studied here, these results highlight a broader implication: semiconductor-inspired nanoscale architectural design rules can be successfully transferred from lithium-ion to sodium-ion electrochemical systems, even when direct materials translation fails. By controlling geometry, interfacial area, and transport length scales, architecture can compensate for fundamental kinetic limitations imposed by larger, more sluggish charge carriers. This strategy is not limited to sodium and may be extendable to other large-ion systems, such as magnesium or potassium, and to a wide range of transition-metal oxide electrodes.

In the present study, a liquid electrolyte was intentionally employed to simplify interpretation of the architectural effects on ion transport and cycling stability. However, the same nanopore platform is inherently compatible with solid-state electrolytes. Our group has previously developed atomic layer deposition processes for sodium phosphorus oxynitride (NaPON)[23], which exhibit excellent conformality on three-dimensional nanostructures and are therefore well suited for integration into nanopore architectures. The demonstrated success of nanoscale architectural control in both lithium- and sodium-ion systems motivates future efforts to combine these architectures with solid-state electrolytes, enabling fully solid-state sodium-ion microbatteries that exploit semiconductor manufacturing precision to achieve high energy, high power, and long cycle life.

Chapter 5: Conclusions and Future Work

5.1 Solid-State Batteries based on PDOL Electrolyte

Since solid-state electrolytes (SSE) have advantages of nonflammability, dendrite resistance, and anode compatibility over liquid electrolytes, ideal SIBs emerge with SSE integrated into nanostructures. Therefore, next plan is to transfer AAO-confined V_2O_5/Pt nanotube architecture from liquid electrolyte operation to a conformal, in-pore solid polymer electrolyte formed by *in-situ* polymerization of 1,3-dioxolane (DOL). This approach preserves the geometric advantages of the nanopore platform while getting rid of issues of liquid electrolyte and enabling electrolyte integration into a full solid-state microbattery.

The goal is to create a conformal, ionically conductive polymer electrolyte inside AAO nanopores by in-situ ring-opening polymerization of DOL with dissolved Na salt. We hope the solid-state battery system can maintain intimate electronic contact between PDOL electrolyte and γ'-V_2O_5/Pt nanotubes while replacing liquid electrolyte with a mechanically robust solid phase. The solid-state microbattery performance (areal capacity, rate, cycle life) will be demonstrated in comparison with the liquid-electrolyte nanopore devices.

5.1.1 Research Plan on Solid-State Batteries

Conformal in-pore polymerization makes use of AAO's conformality to produce a continuous electrolyte that fills the same nanoscale geometry that enabled fast Na^+ kinetics similar to liquid devices. Ideally, solid polymer electrolyte (SPE) eliminates leakage and reduces parasitic side reactions at the electrode/electrolyte interface, improving safety and enabling packaging for on-chip integration[99,100]. Nanoconfinement should preserve short Na^+ transport lengths and high surface-dominated capacity contribution observed in the nanotube architecture, while a solid

matrix can mechanically stabilize interfaces during cycling. The following research is divided into 4 phases:

1) Precursors preparation and infiltration. Prepare DOL solutions containing 1 M NaTFSI (or alternative Na salts) and a controlled concentration of $Mg(TFSI)_2$ (or alternative strong Lewis acid). Infiltrate AAO nanopore devices (Pt/V_2O_5 nanotubes already fabricated) with the monomer/salt solution under vacuum to ensure full pore filling.

2) In-situ polymerization. Optimize polymerization parameters (temperature, time, initiator concentration, etc) to achieve complete conversion without damaging γ′-V_2O_5 crystalline. If possible, optionally include a small fraction of crosslinker or UV-curable monomer to improve mechanical integrity.

3) Characterization and metrology. The solid-state batteries will be characterized by SEM/TEM, EDS line scans, Raman, and XPS to confirm conformal polymer fill and chemical integrity of γ′-V_2O_5. Electrochemical performance including areal capacity, rate capability, Coulombic efficiency, and cycle life will be tested.

4) Possible technical risks and mitigation. a. If the room-temperature ionic conductivity is low, it may be mitigated by adding plasticizers in small amounts, using composite fillers, or optimizing salt dissociation and polymer microstructure. **b.** Interfacial instability between poly(DOL) and γ′-V_2O_5. Mitigate with ultrathin ALD NaPON or surface functionalization of V_2O_5 to form a stable, low-impedance interface. **c.** Incomplete pore filling or heterogeneous polymerization may be solved by using vacuum infiltration, controlled initiator distribution, and optimized parameters of AAO templates to ensure uniform conversion.

A successful in-pore polymerized DOL SPE will demonstrate a practical route to fully solid-state, semiconductor-manufactured sodium microbatteries that retain the rate and cyclability advantages of the nanotube architecture while enabling safer, more compact, and integrable energy storage for on-chip and microsystem applications.

5.1.2 Preliminary Test for In-Situ Polymerization in AAO

According to the research of our group on polymerization of DOL(1,3-dioxolane)/LiTFSI monomers catalyzed by strong Lewis acid ($Mg(TFSI)_2$)[101], it's possible for us to dissolve the catalyzer in monomers and make the solution infiltrate AAO nanopores, then solid-state electrolyte for SIBs would generate via in-situ polymerization. The publication of our group tested the generation of Li-ion electrolyte, and the in-situ polymerization occurred between two planar electrodes to form a thin film electrolyte, which was different from the nano-confined environment within AAO templates. Therefore, we decided to do DOL(1,3-dioxolane)/LiTFSI monomers polymerizing within AAO templates to ensure if the in-situ polymerization strategy still works in porous structure of nanoscale.

We prepared 1 M LiTFSI in DOL solution. $Mg(TFSI)_2$ (50 mM) was added to the solution as the catalyzer for polymerization. The solution was dropped on the top of AAO to let it infiltrate nanopores by gravity. The AAO filled with DOL solution was put in customized split cell (air-tight) to wait for the polymerization for 3 d. The configuration of the customized split cell is shown in Figure 5.1. The AAO with polymer electrolyte (PDOL/ LiTFSI/ $Mg(TFSI)_2$) was taken out of split cell after polymerization for MALDI-TOF mass spectrometry. The MS spectra in Figure 5.2 display groups of distinct molecular ion peaks. The molecular weight between adjacent main peaks keeps 74 Da which is equal to the MW of DOL monomers ($OCH_2CH_2OCH_2$) during the ring-

opening reaction. This result is consistent with previous search of our group[101], confirming that PDOL electrolyte successfully generated within AAO's nanopores.

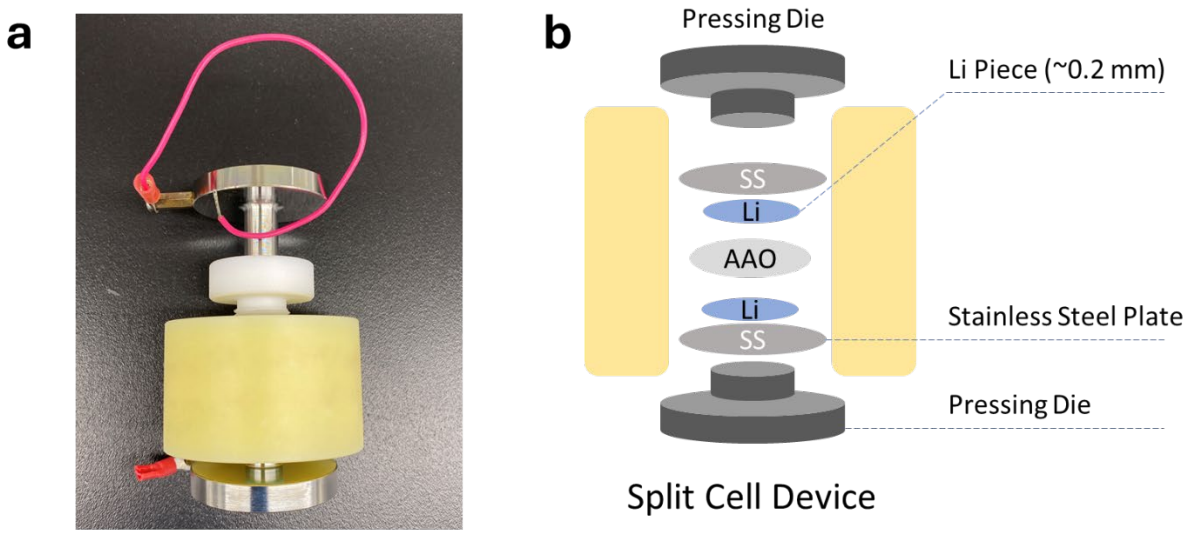

Figure 5.1 a, Picture of the real split cell device. **b,** Inner configuration of the split cell device.

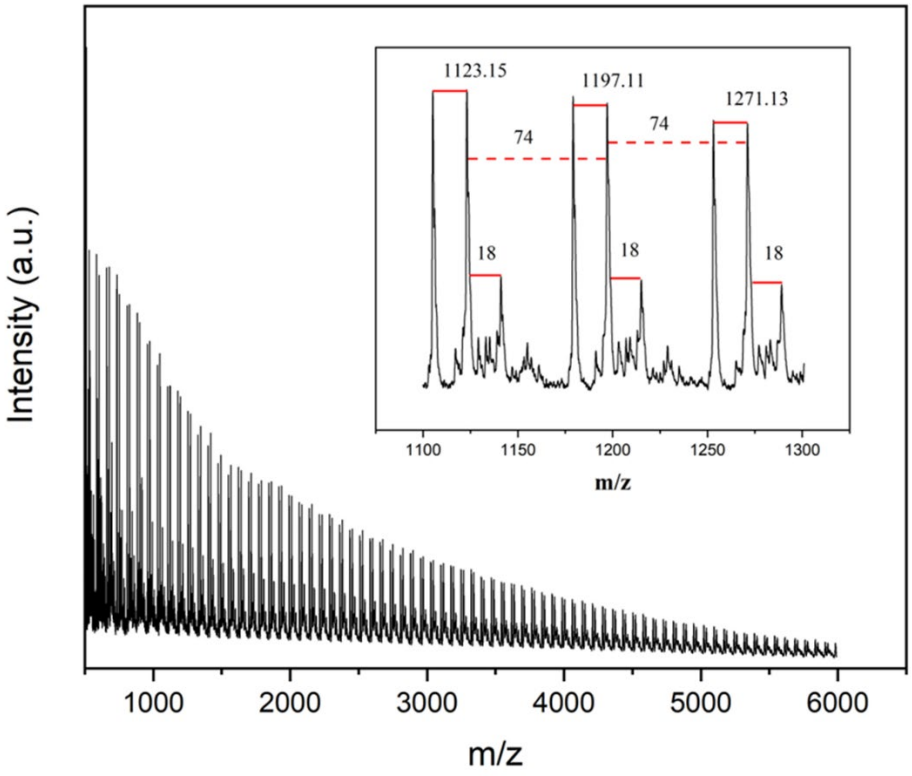

Figure 5.2 MALDI-MS spectra of PDOL electrolyte within AAO nanopores.

Electrochemical measurements were also done for the symmetric solid-state battery to provide more information on in-situ polymerization for us. Electrochemical impedance spectroscopy (EIS) was conducted for the SSB using the range of 1 MHz to 100 mHz with 100 mV amplitude. The EIS (Figure 5.3a) shows characteristic semicircle and tail which represent charge-transfer resistance and semi-infinite diffusion respectively, demonstrating that the in-situ polymerized solid-state electrolyte in AAO's nanopores can constitute a complete battery with electrodes. The large diameter of the semicircle indicates a high interfacial resistance ($> 25\ K\Omega$) within the SSB. GV in Figure 5.3b shows that the charge-discharge cycling only lasts for 15 cycles, which may be caused by the poor contact between the solid-state electrolyte and electrodes. The low current (10 μA) induces high output voltage (~5V vs. Li/Li^+), further confirming the high charge-transfer resistance within the SSB. In conclusion, we've ensured that the in-situ polymerization strategy is effective within nano-confined environments, and it's able to form a workable solid-state battery with electrodes. This part of work paves the way for the following fabrication of solid-state sodium ion batteries.

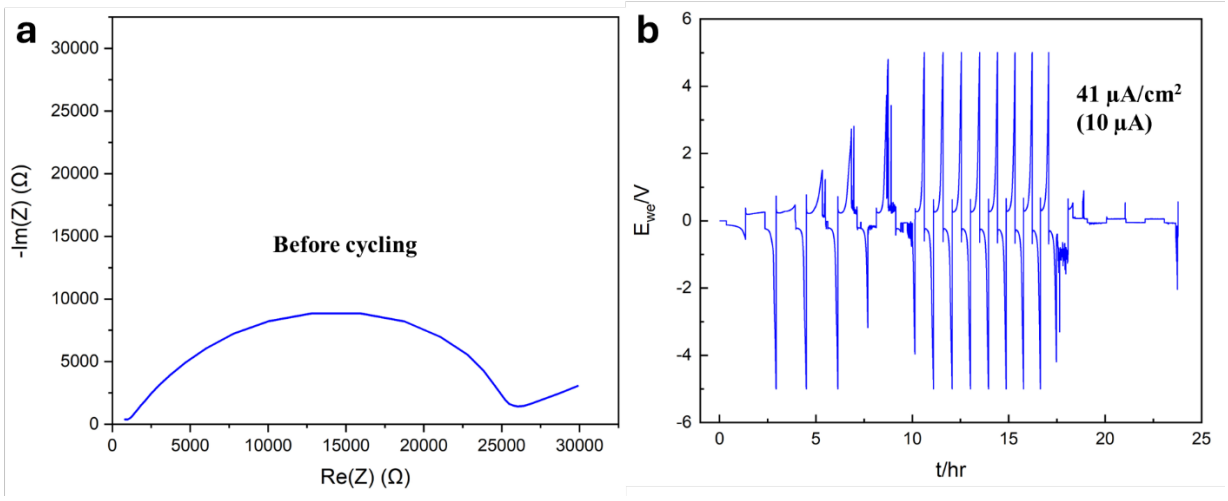

Figure 5.3 Electrochemical measurements for the symmetric solid-state battery a, Nyquist Impedance plot for PDOL (50 mM $Mg(TFSI)_2$ + 1 M LiTFSI in DOL) polymer electrolyte filling AAO which is sandwiched between two Li electrodes. The polymer is 40 μm thick, EIS recorded

between 1 MHz and 100 mHz with 100 mV amplitude. **b,** Charge-discharge cycling of the symmetric solid-state battery under a constant current (10 μA). The battery was short after 15 cycles.

5.2 Integration of NaPON into Three-Dimensional Nanostructure

In addition to PDOL, using conformal NaPON by ALD as the solid electrolyte is another choice for us to transfer AAO platform into a fully solid-state sodium-ion microbattery. This pathway keeps the same semiconductor-manufacturing compatibility and conformality similar to the liquid-electrolyte nanopore devices while targeting the higher safety, integration, and mechanical stability of an inorganic solid electrolyte.

Our goals for the solid-state batteries based on NaPON electrolyte include **a,** deposit conformal NaPON inside AAO nanopores to form a continuous, pinhole-free solid electrolyte layer connecting the γ′-V_2O_5 active material and the counter electrode; **b,** preserve intimate electronic contact via the Pt current collector while preventing electronic leakage through the electrolyte; and **c,** demonstrate solid-state microbattery performance (areal capacity, rate, cycle life) that approaches the liquid-electrolyte baseline and shows improved safety and packaging compatibility.

ALD conformality enables uniform NaPON coverage on high-aspect-ratio nanopores, ensuring continuous ionic pathways and robust interfacial contact in the same geometry that produced high surface-dominated charge storage. Inorganic NaPON offers higher mechanical modulus and thermal stability than polymer electrolytes, which can reduce interfacial degradation and dendrite risk in confined geometries. Since ALD NaPON is compatible with semiconductor processing, it can be easily integrated into wafer-scale microbattery fabrication flows. The following research includes these parts:

1) Process development on planar test structures. Optimize ALD precursors and deposition conditions for NaPON on planar Si wafers to make test samples to investigate growth rate, stoichiometry, and ionic conductivity. Characterize film density, composition (by XPS), and ionic conductivity (by EIS) as a function of deposition temperature and cycle count.

2) Conformal deposition in AAO nanopores. Transfer optimized ALD recipe to AAO nanopore devices with pre-deposited Pt and γ′-V_2O_5 nanotubes. Tune thickness to balance ionic conductivity and electronic blocking, and avoid pore occlusion while ensuring continuous coverage.

3) Characterization and electrochemical testing. Morphology will be characterized by cross-section SEM/TEM and EDS line scans to confirm conformal NaPON coverage. Ionic transport will be investigated by EIS and DC polarization to extract ionic conductivity and Na^+ transference number. Electrochemical performance includes measurements of areal capacity, rate capability, Coulombic efficiency, and cycle life.

4) Possible issues and optimization. a, if pore clogging or loss of accessible surface area occurs, reduce NaPON thickness or use AAO templates with larger pores. **b,** if high interfacial impedance exists between NaPON and γ′-V_2O_5, we can introduce ultrathin ALD interlayers, tune NaPON stoichiometry, and apply low-temperature anneals to improve contact without degrading V_2O_5. **c,** the possible insufficient ionic conductivity at room temperature requires optimizing NaPON composition and deposition parameters, or considering composite approaches (thin ceramic fillers) if needed.

Implementing NaPON via ALD process within the nano-confined 3D porous architecture offers a complementary solid-state route to the in-pore polymerization approach. Success on either

pathway would demonstrate that semiconductor-manufactured 3D architectures can be paired with conformal solid electrolytes to produce safe, integrable, high-performance sodium-ion microbatteries suitable for on-chip and microsystem energy storage.

5.3 Publications During Doctoral Degree

(1) **Sun, Z.**; Kim, N. S.; Tiwari, R.; Zitoun, D.; Rubloff, G. W.; Lee, S. B.; Gregorczyk, K. E. Electrochemical Phase Engineering of Γ′-V2O5 Thin Films for Sodium-Ion Storage Electrodes. *ACS Omega* **2025**, *10* (50), 61414–61421. https://doi.org/10.1021/acsomega.5c06197.

(2) **Sun, Z.**; Kim, N. S.; Lee, S. B.; Rubloff, G. W.; Gregorczyk, K. E. A Three-Dimensional Nanopore Architecture Enabling Stable, High-Power Sodium-Ion Microbatteries. (under review)

(3) J. Gomez, O.; Antar, A.; T. Hall, A.; Tapia-Aracayo, L.; Seo, J.; Kim, N.; **Sun, Z.**; Lim, R.; Chen, F.; Li, Y.; Cumings, J.; Rubloff, G.; Bok Lee, S.; Stewart, D.; Wang, Y. A Facile Synthesis of Bulk LiPON in Solution for Solid-State Electrolytes. *J. Mater. Chem. A* **2025**, *13* (34), 28368–28376. https://doi.org/10.1039/D5TA03196F.
Contributions: Performed SEM and EDS analysis on samples.

Bibliography

(1) Li, W.; Guo, Z.; Yang, J.; Li, Y.; Sun, X.; He, H.; Li, S.; Zhang, J. Advanced Strategies for Stabilizing Single-Atom Catalysts for Energy Storage and Conversion. *Electrochem. Energy Rev.* **2022**, *5* (3), 9. https://doi.org/10.1007/s41918-022-00169-z.

(2) Chen, Y.; Zhang, J.; Yang, L.; Wang, X.; Wu, Q.; Hu, Z. Recent Advances in Non-Precious Metal–Nitrogen–Carbon Single-Site Catalysts for CO2 Electroreduction Reaction to CO. *Electrochem. Energy Rev.* **2022**, *5* (4), 11. https://doi.org/10.1007/s41918-022-00156-4.

(3) Nayak, P. K.; Yang, L.; Brehm, W.; Adelhelm, P. From Lithium-Ion to Sodium-Ion Batteries: Advantages, Challenges, and Surprises. *Angew. Chem. Int. Ed.* **2018**, *57* (1), 102–120. https://doi.org/10.1002/anie.201703772.

(4) Zhou, Q.; Wang, L.; Li, W.; Zhao, K.; Liu, M.; Wu, Q.; Yang, Y.; He, G.; Parkin, I. P.; Shearing, P. R.; Brett, D. J. L.; Zhang, J.; Sun, X. Sodium Superionic Conductors (NASICONs) as Cathode Materials for Sodium-Ion Batteries. *Electrochem. Energy Rev.* **2021**, *4* (4), 793–823. https://doi.org/10.1007/s41918-021-00120-8.

(5) Vaalma, C.; Buchholz, D.; Weil, M.; Passerini, S. A Cost and Resource Analysis of Sodium-Ion Batteries. *Nat. Rev. Mater.* **2018**, *3* (4), 18013. https://doi.org/10.1038/natrevmats.2018.13.

(6) He, M.; Liu, S.; Wu, J.; Zhu, J. Review of Cathode Materials for Sodium-Ion Batteries. *Prog. Solid State Chem.* **2024**, *74*, 100452. https://doi.org/10.1016/j.progsolidstchem.2024.100452.

(7) Slater, M. D.; Kim, D.; Lee, E.; Johnson, C. S. Sodium-Ion Batteries. *Adv. Funct. Mater.* **2013**, *23* (8), 947–958. https://doi.org/10.1002/adfm.201200691.

(8) Perveen, T.; Siddiq, M.; Shahzad, N.; Ihsan, R.; Ahmad, A.; Shahzad, M. I. Prospects in Anode Materials for Sodium Ion Batteries - A Review. *Renew. Sustain. Energy Rev.* **2020**, *119*, 109549. https://doi.org/10.1016/j.rser.2019.109549.

(9) Deng, C.; Zhang, S.; Wang, H.; Zhang, G. "Bubble-in-Nanorod" Hierarchical Hybrid Fiber: A Highly-Efficient Design for Pyrophosphate-Based Freestanding Cathodes towards Fast Sodium/Lithium Intercalation. *Nano Energy* **2018**, *49*, 419–433. https://doi.org/10.1016/j.nanoen.2018.05.008.

(10) Zhan, R.; Zhang, Y.; Chen, H.; Xu, Q.; Ma, Q.; Gao, W.; Yang, T.; Jiang, J.; Bao, S.; Xu, M. High-Rate and Long-Life Sodium-Ion Batteries Based on Sponge-like Three-Dimensional Porous Na-Rich Ferric Pyrophosphate Cathode Material. *ACS Appl. Mater. Interfaces* **2019**, *11* (5), 5107–5113. https://doi.org/10.1021/acsami.8b19874.

(11) Shen, B.; Xu, M.; Niu, Y.; Han, J.; Lu, S.; Jiang, J.; Li, Y.; Dai, C.; Hu, L.; Li, C. Sodium-Rich Ferric Pyrophosphate Cathode for Stationary Room-Temperature Sodium-Ion Batteries. *ACS Appl. Mater. Interfaces* **2018**, *10* (1), 502–508. https://doi.org/10.1021/acsami.7b13516.

(12) Gupta, B.; Hossain, Md. A.; Riaz, A.; Sharma, A.; Zhang, D.; Tan, H. H.; Jagadish, C.; Catchpole, K.; Hoex, B.; Karuturi, S. Recent Advances in Materials Design Using Atomic Layer Deposition for Energy Applications. *Adv. Funct. Mater.* **2022**, *32* (3), 2109105. https://doi.org/10.1002/adfm.202109105.

(13) Sinha, S.; Didwal, P. N.; Nandi, D. K.; Cho, J. Y.; Kim, S.-H.; Park, C.-J.; Heo, J. Atomic Layer Deposited-ZnO@3D-Ni-Foam Composite for Na-Ion Battery Anode: A Novel Route for Easy and Efficient Electrode Preparation. *Ceram. Int.* **2019**, *45* (1), 1084–1092. https://doi.org/10.1016/j.ceramint.2018.09.289.

(14) Yu, F.; Du, L.; Zhang, G.; Su, F.; Wang, W.; Sun, S. Electrode Engineering by Atomic Layer Deposition for Sodium-Ion Batteries: From Traditional to Advanced Batteries. *Adv. Funct. Mater.* **2020**, *30* (9), 1906890. https://doi.org/10.1002/adfm.201906890.
(15) Lee, M.; Ahmad, W.; Kim, D. W.; Kwon, K. M.; Kwon, H. Y.; Jang, H.-B.; Noh, S.-W.; Kim, D.-H.; Zaidi, S. J. A.; Park, H.; Lee, H. C.; Abdul Basit, M.; Park, T. J. Powder Coatings via Atomic Layer Deposition for Batteries: A Review. *Chem. Mater.* **2022**, *34* (8), 3539–3587. https://doi.org/10.1021/acs.chemmater.1c02944.
(16) Chu, S.; Jia, X.; Wang, J.; Liao, K.; Zhou, W.; Wang, Y.; Shao, Z. Reduced Air Sensitivity and Improved Electrochemical Stability of P2–Na2/3Mn1/2Fe1/4Co1/4O2 through Atomic Layer Deposition-Assisted Al2O3 Coating. *Compos. Part B Eng.* **2019**, *173*, 106913. https://doi.org/10.1016/j.compositesb.2019.106913.
(17) Pearse, A.; Schmitt, T.; Sahadeo, E.; Stewart, D. M.; Kozen, A.; Gerasopoulos, K.; Talin, A. A.; Lee, S. B.; Rubloff, G. W.; Gregorczyk, K. E. Three-Dimensional Solid-State Lithium-Ion Batteries Fabricated by Conformal Vapor-Phase Chemistry. *ACS Nano* **2018**, *12* (5), 4286–4294. https://doi.org/10.1021/acsnano.7b08751.
(18) Liu, C.; Kim, N.; Rubloff, G. W.; Lee, S. B. High Performance Asymmetric V 2 O 5–SnO 2 Nanopore Battery by Atomic Layer Deposition. *Nanoscale* **2017**, *9* (32), 11566–11573.
(19) Liu, C.; Gillette, E. I.; Chen, X.; Pearse, A. J.; Kozen, A. C.; Schroeder, M. A.; Gregorczyk, K. E.; Lee, S. B.; Rubloff, G. W. An All-in-One Nanopore Battery Array. *Nat. Nanotechnol.* **2014**, *9* (12), 1031–1039. https://doi.org/10.1038/nnano.2014.247.
(20) Li, S. X.; Kim, N. S.; McKelvey, K.; Liu, C.; White, H. S.; Rubloff, G. W.; Lee, S. B.; Reed, M. A. Enhancing Lithium Insertion with Electrostatic Nanoconfinement in a Lithography Patterned Precision Cell. *ACS Nano* **2019**, *13* (7), 8481–8489. https://doi.org/10.1021/acsnano.9b04390.
(21) Kim, N.; Sahadeo, E.; Liu, C.; Rose, O.; Rubloff, G.; Lee, S. B. Impact of Pore Size, Interconnections, and Dynamic Conductivity on the Electrochemistry of Vanadium Pentoxide in Well Defined Porous Structures. *Phys. Chem. Chem. Phys.* **2018**, *20* (47), 29708–29716. https://doi.org/10.1039/C8CP04706E.
(22) Jarry, A.; Walker, M.; Theodoru, S.; Brillson, L. J.; Rubloff, G. W. Elucidating Structural Transformations in LixV2O5 Electrochromic Thin Films by Multimodal Spectroscopies. *Chem. Mater.* **2020**, *32* (17), 7226–7236. https://doi.org/10.1021/acs.chemmater.0c01478.
(23) Nuwayhid, R. B.; Jarry, A.; Rubloff, G. W.; Gregorczyk, K. E. Atomic Layer Deposition of Sodium Phosphorus Oxynitride: A Conformal Solid-State Sodium-Ion Conductor. *ACS Appl. Mater. Interfaces* **2020**, *12* (19), 21641–21650. https://doi.org/10.1021/acsami.0c03578.
(24) Yang, H.; Jing, M.; Wang, L.; Xu, H.; Yan, X.; He, X. PDOL-Based Solid Electrolyte Toward Practical Application: Opportunities and Challenges. *Nano-Micro Lett.* **2024**, *16* (1), 127. https://doi.org/10.1007/s40820-024-01354-z.
(25) Wu, Y.; Shuang, W.; Wang, Y.; Chen, F.; Tang, S.; Wu, X.-L.; Bai, Z.; Yang, L.; Zhang, J. Recent Progress in Sodium-Ion Batteries: Advanced Materials, Reaction Mechanisms and Energy Applications. *Electrochem. Energy Rev.* **2024**, *7* (1), 17. https://doi.org/10.1007/s41918-024-00215-y.
(26) Rostami, H.; Valio, J.; Suominen, P.; Tynjälä, P.; Lassi, U. Advancements in Cathode Technology, Recycling Strategies, and Market Dynamics: A Comprehensive Review of Sodium Ion Batteries. *Chem. Eng. J.* **2024**, *495*, 153471. https://doi.org/10.1016/j.cej.2024.153471.

(27) Berthelot, R.; Carlier, D.; Delmas, C. Electrochemical Investigation of the P2–NaxCoO2 Phase Diagram. *Nat. Mater.* **2011**, *10* (1), 74–80. https://doi.org/10.1038/nmat2920.
(28) Zhang, X.; Chen, H.; Liu, W.; Xiao, N.; Zhang, Q.; Rui, X.; Huang, S. A Long-Cycling Aqueous Zinc-Ion Pouch Cell: NASICON-Type Material and Surface Modification. *Chem. – Asian J.* **2020**, *15* (9), 1430–1435. https://doi.org/10.1002/asia.202000162.
(29) Su, C. W.; Shao, X.; Jia, Z.; Nepal, R.; Umar, M.; Qin, M. The Rise of Green Energy Metal: Could Lithium Threaten the Status of Oil? *Energy Econ.* **2023**, *121*, 106651. https://doi.org/10.1016/j.eneco.2023.106651.
(30) Du, M.; Li, K.; Yu, N.; Hao, Z.-L.; Guo, J.-Z.; Liang, H.-J.; Gu, Z.-Y.; Zhang, X.-H.; Zhang, K.-Y.; Liu, Y.; Yang, J.-L.; Liu, Y.-T.; Wu, X.-L. Ultrafast Preparation of High-Entropy NASICON Cathode Enables Stabilized Multielectron Redox and Wide-Temperature (−50–60 °C) Workability in Sodium-Ion Batteries. *Adv. Mater.* **2025**, *37* (9), 2418219. https://doi.org/10.1002/adma.202418219.
(31) Gu, Z.-Y.; Wang, X.-T.; Heng, Y.-L.; Liu, Y.; Zheng, S.-H.; Zhang, K.-Y.; Hao, Z.-L.; Wu, X.-L. Polyanionic Cathodes for Sodium-Ion Batteries: Materials, Working Mechanism, and Applications. *Mater. Sci. Eng. R Rep.* **2025**, *165*, 101008. https://doi.org/10.1016/j.mser.2025.101008.
(32) Yabuuchi, N.; Kubota, K.; Dahbi, M.; Komaba, S. Research Development on Sodium-Ion Batteries. *Chem. Rev.* **2014**, *114* (23), 11636–11682. https://doi.org/10.1021/cr500192f.
(33) Gao, L.; Chen, S.; Zhang, L.; Yang, X. Self-Supported Na0.7CoO2 Nanosheet Arrays as Cathodes for High Performance Sodium Ion Batteries. *J. Power Sources* **2018**, *396*, 379–385. https://doi.org/10.1016/j.jpowsour.2018.06.047.
(34) Sun, X.; Fang, W.; Gao, X.; An, H.; Si, J.; Wei, H. Dynamic Interactions among New Energy Metals and Price Adjustment Strategies: A Cross-Industry Chain Perspective. *Energy* **2024**, *303*, 131923. https://doi.org/10.1016/j.energy.2024.131923.
(35) Song, J.; Wang, L.; Lu, Y.; Liu, J.; Guo, B.; Xiao, P.; Lee, J.-J.; Yang, X.-Q.; Henkelman, G.; Goodenough, J. B. Removal of Interstitial H2O in Hexacyanometallates for a Superior Cathode of a Sodium-Ion Battery. *J. Am. Chem. Soc.* **2015**, *137* (7), 2658–2664. https://doi.org/10.1021/ja512383b.
(36) Li, W.-J.; Han, C.; Cheng, G.; Chou, S.-L.; Liu, H.-K.; Dou, S.-X. Chemical Properties, Structural Properties, and Energy Storage Applications of Prussian Blue Analogues. *Small* **2019**, *15* (32), 1900470. https://doi.org/10.1002/smll.201900470.
(37) He, M.; Davis, R.; Chartouni, D.; Johnson, M.; Abplanalp, M.; Troendle, P.; Suetterlin, R.-P. Assessment of the First Commercial Prussian Blue Based Sodium-Ion Battery. *J. Power Sources* **2022**, *548*, 232036. https://doi.org/10.1016/j.jpowsour.2022.232036.
(38) Wei, Q.; DeBlock, R. H.; Butts, D. M.; Choi, C.; Dunn, B. Pseudocapacitive Vanadium-Based Materials toward High-Rate Sodium-Ion Storage. *ENERGY Environ. Mater.* **2020**, *3* (3), 221–234. https://doi.org/10.1002/eem2.12131.
(39) Zhang, Y.; Chen, Y.; Jiang, Y.; Wang, J.; Zheng, X.; Han, B.; Xia, K.; Gao, Q.; Cai, Z.; Zhou, C.; Sun, R. Construction of VS2/VOx Heterostructure via Hydrolysis-Oxidation Coupling Reaction with Superior Sodium Storage Properties. *Adv. Funct. Mater.* **2023**, *33* (12), 2212785. https://doi.org/10.1002/adfm.202212785.
(40) Galy, J. Vanadium Pentoxide and Vanadium Oxide Bronzes—Structural Chemistry of Single (S) and Double (D) Layer *M*xV2O5 Phases. *J. Solid State Chem.* **1992**, *100* (2), 229–245. https://doi.org/10.1016/0022-4596(92)90097-F.

(41) Mukherjee, A.; Sa, N.; Phillips, P. J.; Burrell, A.; Vaughey, J.; Klie, R. F. Direct Investigation of Mg Intercalation into the Orthorhombic V2O5 Cathode Using Atomic-Resolution Transmission Electron Microscopy. *Chem. Mater.* **2017**, *29* (5), 2218–2226. https://doi.org/10.1021/acs.chemmater.6b05089.
(42) Christensen, C. K.; Sørensen, D. R.; Hvam, J.; Ravnsbæk, D. B. Structural Evolution of Disordered LixV2O5 Bronzes in V2O5 Cathodes for Li-Ion Batteries. *Chem. Mater.* **2019**, *31* (2), 512–520. https://doi.org/10.1021/acs.chemmater.8b04558.
(43) Song, H.; Liu, C.; Zhang, C.; Cao, G. Self-Doped V4+–V2O5 Nanoflake for 2 Li-Ion Intercalation with Enhanced Rate and Cycling Performance. *Nano Energy* **2016**, *22*, 1–10. https://doi.org/10.1016/j.nanoen.2016.02.004.
(44) Delmas, C.; Brèthes, S.; Ménétrier, M. ω-LixV2O5 — a New Electrode Material for Rechargeable Lithium Batteries. *J. Power Sources* **1991**, *34* (2), 113–118. https://doi.org/10.1016/0378-7753(91)85030-Z.
(45) Yue, Y.; Liang, H. Micro- and Nano-Structured Vanadium Pentoxide (V2O5) for Electrodes of Lithium-Ion Batteries. *Adv. Energy Mater.* **2017**, *7* (17), 1602545. https://doi.org/10.1002/aenm.201602545.
(46) West, K.; Zachau-Christiansen, B.; Jacobsen, T.; Skaarup, S. Sodium Insertion in Vanadium Oxides. *Solid State Ion.* **1988**, *28–30*, 1128–1131. https://doi.org/10.1016/0167-2738(88)90343-8.
(47) Muller-Bouvet, D.; Baddour-Hadjean, R.; Tanabe, M.; Huynh, L. T. N.; Le, M. L. P.; Pereira-Ramos, J. P. Electrochemically Formed α'-NaV2O5: A New Sodium Intercalation Compound. *Electrochimica Acta* **2015**, *176*, 586–593. https://doi.org/10.1016/j.electacta.2015.07.030.
(48) Baddour-Hadjean, R.; Huynh, L. T. N.; Emery, N.; Pereira-Ramos, J. P. Lithium Insertion in A′-NaV2O5: Na-Pillaring Effect on the Structural and Electrochemical Properties. *Electrochimica Acta* **2018**, *270*, 224–235. https://doi.org/10.1016/j.electacta.2018.03.087.
(49) Baddour-Hadjean, R.; Safrany Renard, M.; Pereira-Ramos, J.-P. Enhanced Electrochemical Properties of Ball-Milled Γ′-V2O5 as Cathode Material for Na-Ion Batteries: A Structural and Kinetic Investigation. *J. Power Sources* **2021**, *482*, 229017. https://doi.org/10.1016/j.jpowsour.2020.229017.
(50) Safrany Renard, M.; Emery, N.; Baddour-Hadjean, R.; Pereira-Ramos, J.-P. γ'-V2O5: A New High Voltage Cathode Material for Sodium-Ion Battery. *Electrochimica Acta* **2017**, *252*, 4–11. https://doi.org/10.1016/j.electacta.2017.08.175.
(51) Safrany Renard, M.; Baddour-Hadjean, R.; Pereira-Ramos, J. P. Kinetic Insight into the Electrochemical Sodium Insertion-Extraction Mechanism of the Puckered Γ′-V2O5 Polymorph. *Electrochimica Acta* **2019**, *322*, 134670. https://doi.org/10.1016/j.electacta.2019.134670.
(52) Batyrbekuly, D.; Laïk, B.; Bakenov, Z.; Bhatia, A.; Pereira-Ramos, J.-P.; Baddour-Hadjean, R. Unlocking the Charge Efficiency of γ'-V2O5 for Na-Ion Battery through a Solution Synthesis Technique. *Acta Mater.* **2025**, *282*, 120461. https://doi.org/10.1016/j.actamat.2024.120461.
(53) Chen, X.; Pomerantseva, E.; Banerjee, P.; Gregorczyk, K.; Ghodssi, R.; Rubloff, G. Ozone-Based Atomic Layer Deposition of Crystalline V2O5 Films for High Performance Electrochemical Energy Storage. *Chem. Mater.* **2012**, *24* (7), 1255–1261. https://doi.org/10.1021/cm202901z.

(54) Trócoli, R.; Parajuli, P.; Frontera, C.; Black, A. P.; Alexander, G. C. B.; Roy, I.; Arroyo-de Dompablo, M. E.; Klie, R. F.; Cabana, J.; Palacín, M. R. β-V2O5 as Magnesium Intercalation Cathode. *ACS Appl. Energy Mater.* **2022**, *5* (10), 11964–11969. https://doi.org/10.1021/acsaem.2c02371.
(55) Oudenhoven, J. F. M.; Baggetto, Loïc.; Notten, P. H. L. All-Solid-State Lithium-Ion Microbatteries: A Review of Various Three-Dimensional Concepts. *Adv. Energy Mater.* **2011**, *1* (1), 10–33. https://doi.org/10.1002/aenm.201000002.
(56) Cras, F. L.; Pecquenard, B.; Dubois, V.; Phan, V.-P.; Guy-Bouyssou, D. All-Solid-State Lithium-Ion Microbatteries Using Silicon Nanofilm Anodes: High Performance and Memory Effect. *Adv. Energy Mater.* **2015**, *5* (19), 1501061. https://doi.org/10.1002/aenm.201501061.
(57) Dudney, N. J. Solid-State Thin-Film Rechargeable Batteries. *Mater. Sci. Eng. B* **2005**, *116* (3), 245–249. https://doi.org/10.1016/j.mseb.2004.05.045.
(58) White, R. J.; White, H. S. Electrochemistry in Nanometer-Wide Electrochemical Cells. *Langmuir* **2008**, *24* (6), 2850–2855. https://doi.org/10.1021/la7031779.
(59) Petersen, M. K.; Kumar, R.; White, H. S.; Voth, G. A. A Computationally Efficient Treatment of Polarizable Electrochemical Cells Held at a Constant Potential. *J. Phys. Chem. C* **2012**, *116* (7), 4903–4912. https://doi.org/10.1021/jp210252g.
(60) Vaalma, C.; Buchholz, D.; Weil, M.; Passerini, S. A Cost and Resource Analysis of Sodium-Ion Batteries. *Nat. Rev. Mater.* **2018**, *3* (4), 18013. https://doi.org/10.1038/natrevmats.2018.13.
(61) Zhao, weimin; Wang, M.; Lin, H.; Kim, K.; He, R.; Feng, S.; Liu, H. Research Progress on Electrolyte Key Salts for Sodium-Ion Batteries. *Prog. Nat. Sci. Mater. Int.* **2024**, *34* (2), 263–273. https://doi.org/10.1016/j.pnsc.2024.03.003.
(62) He, L.; Guo, J.; Liu, S.; Wang, F.; Li, X.; Su, Z. Progress of Metal Phosphides as the Anode Materials for Sodium Ion Batteries. *J. Alloys Compd.* **2024**, *997*, 174924. https://doi.org/10.1016/j.jallcom.2024.174924.
(63) Nuwayhid, R. B.; Jarry, A.; Rubloff, G. W.; Gregorczyk, K. E. Atomic Layer Deposition of Sodium Phosphorus Oxynitride: A Conformal Solid-State Sodium-Ion Conductor. *ACS Appl. Mater. Interfaces* **2020**, *12* (19), 21641–21650. https://doi.org/10.1021/acsami.0c03578.
(64) Hosono, E.; Saito, T.; Hoshino, J.; Okubo, M.; Saito, Y.; Nishio-Hamane, D.; Kudo, T.; Zhou, H. High Power Na-Ion Rechargeable Battery with Single-Crystalline Na0.44MnO2 Nanowire Electrode. *J. Power Sources* **2012**, *217*, 43–46. https://doi.org/10.1016/j.jpowsour.2012.05.100.
(65) Duan, W.; Zhu, Z.; Li, H.; Hu, Z.; Zhang, K.; Cheng, F.; Chen, J. Na3V2(PO4)3@C Core–Shell Nanocomposites for Rechargeable Sodium-Ion Batteries. *J. Mater. Chem. A* **2014**, *2* (23), 8668–8675. https://doi.org/10.1039/C4TA00106K.
(66) Zhao, L.; Liu, X.; Li, J.; Diao, X.; Zhang, J. One–Step Synthesis of Three–Dimensional Na3V2(PO4)3/Carbon Frameworks as Promising Sodium–Ion Battery Cathode. *Nanomaterials* **2023**, *13* (3), 446. https://doi.org/10.3390/nano13030446.
(67) Batyrbekuly, D.; Laïk, B.; Bakenov, Z.; Bhatia, A.; Pereira-Ramos, J.-P.; Baddour-Hadjean, R. Unlocking the Charge Efficiency of γ'-V2O5 for Na-Ion Battery through a Solution Synthesis Technique. *Acta Mater.* **2025**, *282*, 120461. https://doi.org/10.1016/j.actamat.2024.120461.
(68) Sun, Z.; Kim, N. S.; Tiwari, R.; Zitoun, D.; Rubloff, G. W.; Lee, S. B.; Gregorczyk, K. E. Electrochemical Phase Engineering of Γ′-V2O5 Thin Films for Sodium-Ion Storage

Electrodes. *ACS Omega* **2025**, *10* (50), 61414–61421. https://doi.org/10.1021/acsomega.5c06197.
(69) Zhang, T.; Wang, T.; Zheng, Y.; Qian, L.; Liu, X.; Yan, W.; Zhang, J. Atomic Layer Deposition for Sodium-Ion Batteries. *Adv. Energy Mater. n/a* (n/a), e01760. https://doi.org/10.1002/aenm.202501760.
(70) Plečkaitytė, G.; Petrulevičienė, M.; Staišiūnas, L.; Tediashvili, D.; Pilipavičius, J.; Juodkazytė, J.; Vilčiauskas, L. Understanding and Mitigation of NaTi2(PO4)3 Degradation in Aqueous Na-Ion Batteries. *J. Mater. Chem. A* **2021**, *9* (21), 12670–12683. https://doi.org/10.1039/D1TA01215K.
(71) Ren, W.; Zhou, W.; Zhang, H.; Cheng, C. ALD TiO2-Coated Flower-like MoS2 Nanosheets on Carbon Cloth as Sodium Ion Battery Anode with Enhanced Cycling Stability and Rate Capability. *ACS Appl. Mater. Interfaces* **2017**, *9* (1), 487–495. https://doi.org/10.1021/acsami.6b13179.
(72) Sinha, S.; Didwal, P. N.; Nandi, D. K.; Cho, J. Y.; Kim, S.-H.; Park, C.-J.; Heo, J. Atomic Layer Deposited-ZnO@3D-Ni-Foam Composite for Na-Ion Battery Anode: A Novel Route for Easy and Efficient Electrode Preparation. *Ceram. Int.* **2019**, *45* (1), 1084–1092. https://doi.org/10.1016/j.ceramint.2018.09.289.
(73) Staišiūnas, L.; Pilipavičius, J.; Tediashvili, D.; Juodkazytė, J.; Vilčiauskas, L. Engineering of Conformal Electrode Coatings by Atomic Layer Deposition for Aqueous Na-Ion Battery Electrodes. *J. Electrochem. Soc.* **2023**, *170* (5), 050533. https://doi.org/10.1149/1945-7111/acd4ee.
(74) Fang, Y.; Yu, X.-Y.; Lou, X. W. (David). A Practical High-Energy Cathode for Sodium-Ion Batteries Based on Uniform P2-Na0.7CoO2 Microspheres. *Angew. Chem.* **2017**, *129* (21), 5895–5899. https://doi.org/10.1002/ange.201702024.
(75) Zhou, P.; Che, Z.; Ma, F.; Zhang, J.; Weng, J.; Wu, X.; Miao, Z.; Lin, H.; Zhou, J.; Zhuo, S. Designing Water/Air-Stable P2-Layered Cathodes with Delayed P2–O2 Phase Transition by Composition and Structure Engineering for Sodium-Ion Batteries at High Voltage. *Chem. Eng. J.* **2021**, *420*, 127667. https://doi.org/10.1016/j.cej.2020.127667.
(76) Zhao, C.; Ding, F.; Lu, Y.; Chen, L.; Hu, Y.-S. High-Entropy Layered Oxide Cathodes for Sodium-Ion Batteries. *Angew. Chem. Int. Ed.* **2020**, *59* (1), 264–269. https://doi.org/10.1002/anie.201912171.
(77) Mukherjee, A.; Ardakani, H. A.; Yi, T.; Cabana, J.; Shahbazian-Yassar, R.; Klie, R. F. Direct Characterization of the Li Intercalation Mechanism into α-V2O5 Nanowires Using in-Situ Transmission Electron Microscopy. *Appl. Phys. Lett.* **2017**, *110* (21), 213903. https://doi.org/10.1063/1.4984111.
(78) Assadi, M. H. N.; Hanaor, D. A. H. Oxygen Redox in Battery Cathodes: A Brief Overview. In *Computational Design of Battery Materials*; Hanaor, D. A. H., Ed.; Springer International Publishing: Cham, 2024; pp 421–435. https://doi.org/10.1007/978-3-031-47303-6_15.
(79) Both, S.; Hein, S.; Danner, T.; Latz, A. Modeling Oxygen Loss and Phase Transformation in Ni-Rich Cathode Materials: Impact of Electrode Microstructure. *Batter. Supercaps* **2025**, *8* (8), e202400802. https://doi.org/10.1002/batt.202400802.
(80) Ramana, C. V.; Smith, R. J.; Hussain, O. M.; Massot, M.; Julien, C. M. Surface Analysis of Pulsed Laser-Deposited V2O5 Thin Films and Their Lithium Intercalated Products Studied by Raman Spectroscopy. *Surf. Interface Anal.* **2005**, *37* (4), 406–411. https://doi.org/10.1002/sia.2018.

(81) Baddour-Hadjean, R.; Golabkan, V.; Pereira-Ramos, J. P.; Mantoux, A.; Lincot, D. A Raman Study of the Lithium Insertion Process in Vanadium Pentoxide Thin Films Deposited by Atomic Layer Deposition. *J. Raman Spectrosc.* **2002**, *33* (8), 631–638. https://doi.org/10.1002/jrs.893.
(82) Baddour-Hadjean, R.; Raekelboom, E.; Pereira-Ramos, J. P. New Structural Characterization of the LixV2O5 System Provided by Raman Spectroscopy. *Chem. Mater.* **2006**, *18* (15), 3548–3556. https://doi.org/10.1021/cm060540g.
(83) Bhatia, A.; Pereira-Ramos, J.-P.; Emery, N.; Baddour-Hadjean, R. Γ′-V2O5 Polymorph as a Promising Host Structure for Potassium Storage: An Electrochemical and Structural Study. *Chem. Mater.* **2021**, *33* (13), 5276–5289. https://doi.org/10.1021/acs.chemmater.1c01390.
(84) Song, H.; Liu, C.; Zhang, C.; Cao, G. Self-Doped V4+–V2O5 Nanoflake for 2 Li-Ion Intercalation with Enhanced Rate and Cycling Performance. *Nano Energy* **2016**, *22*, 1–10. https://doi.org/10.1016/j.nanoen.2016.02.004.
(85) Bayaguud, A.; Zhang, Z.; Geng, M.; Fu, Y.; Yu, Y.; Zhu, C. Transformation of Polyoxometalate into 3D Porous Li-Containing Oxide: A Case Study of γ-LiV2O5 for High-Performance Cathodes of Li-Ion Batteries. *Small Methods* **2019**, *3* (10), 1900187. https://doi.org/10.1002/smtd.201900187.
(86) Hakala, B. V.; Manousou, D. K.; Glazyrin, K.; Crichton, W. A.; Friese, K.; Grzechnik, A. Stability of Wadsley-Type Vanadium Oxides V2O5 and V6O13 at High Pressures. *J. Alloys Compd.* **2022**, *911*, 164966. https://doi.org/10.1016/j.jallcom.2022.164966.
(87) Galy, J.; Satto, C.; Sciau, P.; Millet, P. Atomic Modeling of the $\delta \Leftrightarrow \varepsilon$ LiV2O5 Phase Transition and Simulation of the XRD Powder Pattern Evolution. *J. Solid State Chem.* **1999**, *146* (1), 129–136. https://doi.org/10.1006/jssc.1999.8318.
(88) Anderson, D. N.; Willett, R. D. Refinement of the Structure of LiV2O5. *Acta Crystallogr. B* **1971**, *27* (7), 1476–1477. https://doi.org/10.1107/S0567740871004199.
(89) Bhatia, A.; Xu, J.; Pereira-Ramos, J.-P.; Rousse, G.; Baddour-Hadjean, R. Γ′-V2O5 Polymorph: A Genuine Zn Intercalation Material for Nonaqueous Rechargeable Batteries. *Chem. Mater.* **2022**, *34* (3), 1203–1212. https://doi.org/10.1021/acs.chemmater.1c03739.
(90) Harrington, G. F.; Santiso, J. Back-to-Basics Tutorial: X-Ray Diffraction of Thin Films. *J. Electroceramics* **2021**, *47* (4), 141–163. https://doi.org/10.1007/s10832-021-00263-6.
(91) Dai, J.; Li, S. F. Y.; Gao, Z.; Siow, K. S. Novel Method for Synthesis of γ-Lithium Vanadium Oxide as Cathode Materials in Lithium Ion Batteries. *Chem. Mater.* **1999**, *11* (11), 3086–3090. https://doi.org/10.1021/cm9901461.
(92) Zhang, H.-T.; Zhang, Z.; Zhou, H.; Tanaka, H.; Fong, D. D.; Ramanathan, S. Beyond Electrostatic Modification: Design and Discovery of Functional Oxide Phases via Ionic-Electronic Doping. *Adv. Phys. X* **2019**, *4* (1), 1523686. https://doi.org/10.1080/23746149.2018.1523686.
(93) Sood, A.; Poletayev, A. D.; Cogswell, D. A.; Csernica, P. M.; Mefford, J. T.; Fraggedakis, D.; Toney, M. F.; Lindenberg, A. M.; Bazant, M. Z.; Chueh, W. C. Electrochemical Ion Insertion from the Atomic to the Device Scale. *Nat. Rev. Mater.* **2021**, *6* (9), 847–867. https://doi.org/10.1038/s41578-021-00314-y.
(94) Sun, S.; Han, Z.; Liu, W.; Xia, Q.; Xue, L.; Lei, X.; Zhai, T.; Su, D.; Xia, H. Lattice Pinning in MoO3 via Coherent Interface with Stabilized Li+ Intercalation. *Nat. Commun.* **2023**, *14* (1), 6662. https://doi.org/10.1038/s41467-023-42335-x.

(95) Li, C.; Zang, R.; Li, P.; Man, Z.; Wang, S.; Li, X.; Wu, Y.; Liu, S.; Wang, G. High Crystalline Prussian White Nanocubes as a Promising Cathode for Sodium-Ion Batteries. *Chem. – Asian J.* **2018**, *13* (3), 342–349. https://doi.org/10.1002/asia.201701715.
(96) Ardizzone, S.; Fregonara, G.; Trasatti, S. "Inner" and "Outer" Active Surface of RuO2 Electrodes. *Electrochimica Acta* **1990**, *35* (1), 263–267. https://doi.org/10.1016/0013-4686(90)85068-X.
(97) Wang, J.; Polleux, J.; Lim, J.; Dunn, B. Pseudocapacitive Contributions to Electrochemical Energy Storage in TiO2 (Anatase) Nanoparticles. *J. Phys. Chem. C* **2007**, *111* (40), 14925–14931. https://doi.org/10.1021/jp074464w.
(98) He, M.; Davis, R.; Chartouni, D.; Johnson, M.; Abplanalp, M.; Troendle, P.; Suetterlin, R.-P. Assessment of the First Commercial Prussian Blue Based Sodium-Ion Battery. *J. Power Sources* **2022**, *548*, 232036. https://doi.org/10.1016/j.jpowsour.2022.232036.
(99) Hayashi, A.; Noi, K.; Sakuda, A.; Tatsumisago, M. Superionic Glass-Ceramic Electrolytes for Room-Temperature Rechargeable Sodium Batteries. *Nat. Commun.* **2012**, *3* (1), 856. https://doi.org/10.1038/ncomms1843.
(100) Yu, Z.; Shang, S.-L.; Seo, J.-H.; Wang, D.; Luo, X.; Huang, Q.; Chen, S.; Lu, J.; Li, X.; Liu, Z.-K.; Wang, D. Exceptionally High Ionic Conductivity in Na3P0.62As0.38S4 with Improved Moisture Stability for Solid-State Sodium-Ion Batteries. *Adv. Mater.* **2017**, *29* (16), 1605561. https://doi.org/10.1002/adma.201605561.
(101) Sahadeo, E.; Wang, Y.; Lin, C.-F.; Li, Y.; Rubloff, G.; Lee, S. B. Mg2+ Ion-Catalyzed Polymerization of 1,3-Dioxolane in Battery Electrolytes. *Chem. Commun.* **2020**, *56* (33), 4583–4586. https://doi.org/10.1039/D0CC01769H.